TEXTURE CONTROL BY SELECTIVE DEFORMATION MECHANISM

ACTIVATION IN MAGNESIUM ALLOY

A Dissertation

by

DAVID CHRISTOPHER FOLEY

Submitted to the Office of Graduate and Professional Studies of
Texas A&M University
in partial fulfillment of the requirements for the degree of

DOCTOR OF PHILOSOPHY

Chair of Committee,	K. Ted Hartwig
Committee Members,	Ibrahim Karaman
	Xinghang Zhang
	K. Lee Peddicord
Head of Department,	Ibrahim Karaman

August 2014

Major Subject: Materials Science and Engineering

ABSTRACT

The need for high strength, light weight structures in automotive and aerospace applications has driven a resurgence of interest in magnesium and its alloys. Unlike aluminum, wrought magnesium typically has a high degree of mechanical anisotropy because of its hexagonal close packed structure. Our objectives were to develop high strength (>350MPa yield) in a bulk magnesium alloy using grain refinement and to control the mechanical anisotropy by controlling crystallographic texture. This dissertation covers the development of thermomechanical processing methods used to tailor the strength and anisotropy of a magnesium alloy with 3%Zn and 1%Zr. The areas of focus in this study were as follows.

First, we developed severe deformation processing strategies that increase strength in single-phase Mg alloy via grain refinement to submicron average grain size. We also established the achievable crystallographic textures in Mg alloy using 90° equal channel angular extrusion. In support of these first two goals, we determined the deformation mechanisms activated by differing strain paths and temperatures in single phase Mg alloy. Then, we established the effectiveness of these severe deformation processing strategies on both bar and plate workpiece geometries. We generated a wide range of crystallographic textures using thermomechanical processing. Using this knowledge, we established the effect of grain sizes down to submicron levels on room temperature deformation mechanism activity in single phase Mg alloy.

We accomplished these goals through the use of equal channel angular extrusion, rolling, and heat treatment coupled with microscopy, diffraction, and mechanical testing. Notable achievements include demonstration of tensile twin suppression by grain refinement, the development of quasi-single-crystal textures, and the capacity to generate material with nearly identical texture but a range of grain sizes spanning almost two orders of magnitude. The experiments also supported (and were supported by) the development of visco-plastic self-consistent crystal plasticity modeling predictions thanks to the efforts of my colleagues. This work will further the development of advanced manufacturing and design using wrought Mg alloys.

To my parents.

Thank you.

ACKNOWLEDGEMENTS

TABLE OF CONTENTS

LIST OF FIGURES

LIST OF TABLES

CHAPTER I

INTRODUCTION

For almost a century, magnesium-based products have been used in aerospace
and automotive applications where high strength-to-weight ratios are required. However,
the material does not behave like the steel and aluminum that it competes with. The
hexagonal close packed crystal structure results in a large variation in mechanical
properties based on orientation, especially for wrought products. Further, the
development of high-strength magnesium alloys has not been funded by governments
and corporations on nearly the same level as steel or aluminum, contributing to the
relatively low strength of currently available Mg products. As transportation energy
sources become more expensive, these issues are receiving more attention and funding,
encouraging both traditional and novel methods to improve Mg alloy performance. We
saw an opportunity to make significant improvements to existing alloys by developing
and applying a comprehensive knowledge of Mg alloy deformation mechanisms.

Objectives and Approach

This work began with the goal, set by the U.S. Army Research Laboratory, of
producing high strength magnesium by applying severe plastic deformation to a common
commercially available magnesium alloy. Secondary to this goal was the control of
mechanical anisotropy. That is, the large variation in yield strength in different
directions, or tension/compression in the same direction, typical of wrought Mg and
other hexagonal close-packed (HCP) metals. Both of these goals required an
understanding of the deformation mechanisms in the alloy, including how these

mechanisms are affected by microstructure, texture, strain path, and deformation temperature. Using in-situ and ex-situ diffraction and mechanical testing coupled with microscopy, a range of deformation conditions were examined, leading to a thorough understanding of texture formation and grain refinement. While the initial goal of producing high (unidirectional) strength magnesium was met relatively early in the project, achieving meaningful control over mechanical anisotropy required a deep understanding of Mg deformation mechanisms and the interconnected influences of these mechanisms. Although HCP material can never be truly isotropic, the work presented here demonstrates the capability of well-designed thermomechanical processing to produce material with responses ranging from extreme anisotropy (yield strength ratios greater than 3:1) to a yield anisotropy comparable to typical cubic materials. Since we were able to also control grain size quite well, and produced finer microstructures than previously achieved, we were the first to demonstrate the suppression of yield by tensile twinning at room temperature.

Magnesium

Magnesium was first produced commercially in Germany beginning in the mid-19th century for use in flashbulbs and other applications where the reactive nature of the pure metal was useful [1]. In 1914 the Germans went on a tour of Europe, convincing other countries to begin producing their own magnesium by 1915. However, the Germans still lead development of magnesium alloys and were using them in automobiles and airships by the 1920s. Production and use of Mg in the United States grew significantly when the Germans took a second tour of Europe, with output jumping

2

from 4,500t in 1938 to 160,000t in 1944[1]. However, production rapidly scaled back post-war [2]. Today there is only one primary producer in the United States (although a start-up with a new process has received significant government support in the hopes of commercial viability) and much of worldwide production is in China. While most Western plants have used an electrolytic process to pull Mg from seawater and brine, many Chinese producers utilize a thermal process with an ore starting material. This Pidgeon process uses more energy than electrolysis but results in a higher purity[3]. Although less important for use in Al alloys, minimizing Fe and other impurities has a strong impact on corrosion in Mg alloys, and this often leads to higher corrosion performance of Chinese produced Mg alloys compared to Western equivalents.

Magnesium is most commonly used as an alloying addition to aluminum [4]. However, the second most common use is in Mg alloys for structural applications. Both of these metals are typically used when a high strength-to-weight ratio is required. However, there are other notable characteristics that make Mg preferable in specialty applications for which competing alloys (primarily aluminum and titanium) are unsuited. For example, a 0.5% Zr casting alloy has a damping capacity that is up to 300 times greater than common aluminum alloys [5]. Excellent castability and low shrinkage allow for easier casting of complex or thin parts [6]. Currently, the primary disadvantage of Mg compared to Al is cost. Although cost varies widely from alloy to alloy, primary Mg is currently three times as expensive as Al (weight basis) in the USA [7].

Perhaps the most widely known drawback to Mg is something of a myth perpetrated by high school chemistry teachers; Mg is flammable. The key to the lab

demonstration is that the Mg is in a thin strip, which makes it easy to reach the $>600^{\circ}C$ melting point (the autoignition temperature is just above melting for most Mg alloys). Once on fire, the majority of Mg alloys are not self-extinguishing. Further, conventional fire extinguishing methods will not work, as CO_2 and H_2O serve as an oxygen source. One prominent example of this in history is the worst auto racing accident, the 1955 Le Mans tragedy [8]. The magnesium-bodied Mercedes-Benz that tumbled into spectators caught fire immediately (the fuel tank, along with most of the other components, had ruptured on impact with the track wall). By the time firefighters attempted to douse the flames, the Mg had caught and the addition of water only served to intensify the fire. It is good practice to have a bucket of sand or salt nearby when machining Mg alloys or otherwise creating powders or shavings. Mg alloys also generally perform poorly in corrosive environments, further limiting wider application. There are, however, commercially available alloys with a much lower affinity for oxygen, and currently the Federal Aviation Administration is in the process of approving low-flammability alloys for in-cabin components [9]. Most of these alloys contain Y, which inhibits flammability due to the formation of a surface oxide [10]. Additionally, appropriate design considerations can limit corrosion even in somewhat demanding environments. For example, several naval aircraft gearboxes currently in service are Mg alloy castings. Much like low-alloy steels, a waterproof coating combined with design that avoids standing water will serve to dramatically extend Mg alloy lifespan. The reactivity or pure Mg with oxygen should be thought of more as a reason for alloying and basic corrosion prevention than a dangerous and prohibitive concern.

4

Comparison with Other Materials

With a density of 1.74 g/cc magnesium is a lightweight material often referred to as "the lightest structural metal" [11,12]. While the density of pure Mg is lower than even aluminum, structural Mg is always alloyed. The Mg alloy that this study focuses on, AZ31, is only lightly alloyed and thus has a density of 1.78 g/cc, still slightly under that of beryllium (1.85 g/cc) and much less than aluminum (2.7 g/cc). However, there is an important additional factor to consider: strength. Combining the density and yield strength values, the specific strength of lightweight alloys provides a better indicator of their suitability for lightweight structures. Table 1 lists specific strength ranges for commercially available lightweight metals and alloys, revealing that 7000 series aluminum alloys and Ti-6-4, longtime favorites of aerospace engineers, outperform the lower-density magnesium on a strength-to-weight basis. Even high-strength steel, with a density of 7.84 g/cc, outperforms low-strength Mg alloys. Why, then, does magnesium warrant attention as a high-strength structural material? The next chapter contains a brief review of the strengthening mechanisms in metallic alloys in general with commentary on the significance of each factor to Mg alloys and opportunities for advancement.

Table 1. Specific strengths of commercially available magnesium, steel, titanium, and aluminum alloys illustrating the interplay of strength and density.

Material	Yield Strength (Mpa)	Density (g/cm^3)	Specific Strength (N m/g)	Reference
Mg AZ31B-H24	160	1.78	90	[13]
Mg Elektron 675	310	1.95	159	[14]
Fe AISI 4340	470	7.85	60	[15]
Fe Creusabro 8000	1250	7.85	159	[16]
Ti Titanium 6-4	900	4.42	203	[17]
Al 6061-T6	415	2.70	154	[18]
Al 7075-T6	515	2.81	183	[18]

Improving Mechanical Strength

For any deformation mechanism, atomic displacement is the essential mechanism for a material to yield under stress. This yielding often occurs via dislocation slip but also through twinning, phase change, or grain boundary sliding. The resistance to these activities determines the strength of a metal and there are several microstructural characteristics that impact this resistance. Dislocation motion can be inhibited by grain boundaries, phase boundaries, and the resistance associated with the atomic matrix itself. There are several classical methods by which materials engineers inhibit this displacement to increase yield and ultimate strengths. One of the most common is alloying. While swords crafted from Fe-Ni meteorites were the prized weapons of kings and conquerors of the day [19], the Bronze Age was defined by the alloy that allowed the fabrication of strong, ductile objects. By 4000 BCE man had progressed beyond hammering out pure copper to make tools and began intentionally adding arsenic, which naturally occurred in low concentrations at most copper ore sites, to the copper they cast

into jewelry or hammered into tools [20]. In addition to various other benefits, the arsenic hardened the copper through solid solution strengthening. The alloy of interest in the present study also utilizes solid solution strengthening, the effect of which is represented by Equation 1.

$$\sigma_{ss} = mBc^n \tag{1}$$

This represents the change stress required to move a dislocation in terms of the Taylor orientation factor m, solution hardening rate B, solute concentration c, and n taken as either 1/2 or 2/3. The B term and Taylor factor captures the shear modulus, burgers's vector and modulus change due to lattice distortion surrounding the solute atom. The simplified term is useful when fitting experimental data and establishing Mg solid solution strength. For the 3% Al alloy used in this study (AZ31), c is 0.03, B is estimated to be in the range of 21 MPa(at.)$^{-1/2}$ for n = ½ or 40MPa(at.)$^{-2/3}$ for n = 2/3 [21]. It should be noted, however, that this estimate reflects primarily the impact of alloying on basal slip; it would likely be the only significant contribution to yield at room temperature in a cast material, and will be discussed in the next section. Extracting these values from empirical data requires the subtraction of both the native strength of the Mg matrix and the effect of grain size. These additional parameters are represented in the Hall-Petch equation:

$$\sigma_{HP} = \sigma_0 + kd^{-\frac{1}{2}} \tag{2}$$

Where σ_0 is ~11MPa for pure Mg and k is taken as 0.3 MPa m$^{-1/2}$ of a Mg-Al alloy [21]. A set of samples from the same alloy with similar dislocation density but widely varying grain size can be used to find these values. In this study, room

temperature mechanical properties will be controlled by grain size and texture. Essentially, we will be changing *m* in Equation 1 and *d* in Equation 2. While this may seem straightforward, the complexity of magnesium deformation mechanisms results in the interaction of eight such equations (in addition to other confounding factors) rather than two. A brief overview of these mechanisms is called for before proceeding with the study.

Mg Deformation Mechanisms

There are five major deformation modes in Mg alloys, two of which are twinning. This twinning is necessary because of the insufficient number of independent slip systems to satisfy the von Mises yield criteria. These systems are depicted in Figure 1 with the active slip direction indicated with a red arrow. Basal {0002} slip is the most common AZ31 deformation system at room temperature due to its low critical resolved shear stress and multi-directional nature. At room temperature, the shear stress required for micro-yield is roughly 25MPa [22]. There are three $< 11\bar{2}0 >$ slip directions on this close-packed plane, allowing for similar Schmid factors around the c-axis. These directions are the same in prismatic $\{10\bar{1}0\}$ slip. However, this system is more difficult to activate due in part to the lower packing factor on these planes. Tensile twinning on the $\{10\bar{1}2\}$ plane is also active at room temperature as the critical resolved shear stress is close to that of basal slip. However, this system is unidirectional. The total length along the C-axis of the parent material must extend when twins are formed on this plane. Thus, this is referred to as tensile twinning despite possible activation by compression perpendicular to the C-axis. The twinned material is reoriented at 86° and typically the

8

twin bands begin and end at grain boundaries. This near-perpendicular reorientation often places the twinned material in a "hard" orientation with the c-axis parallel or perpendicular to the loading direction. Therefore, further strain in the twinned material cannot be accommodated by basal or prismatic slip (or a second round of tensile twinning). In this case there may be activation of Pyramidal <c+a> slip. This is on the $\{10\overline{1}0\}$ plane in six directions. Since this requires a relatively large stress at room temperature, other slip systems and tensile twinning will typically continue until the entire microstructure is reoriented in the "hard" direction. Even then, pyramidal slip may not play a significant role; this complete reorientation is usually quickly followed by fracture.
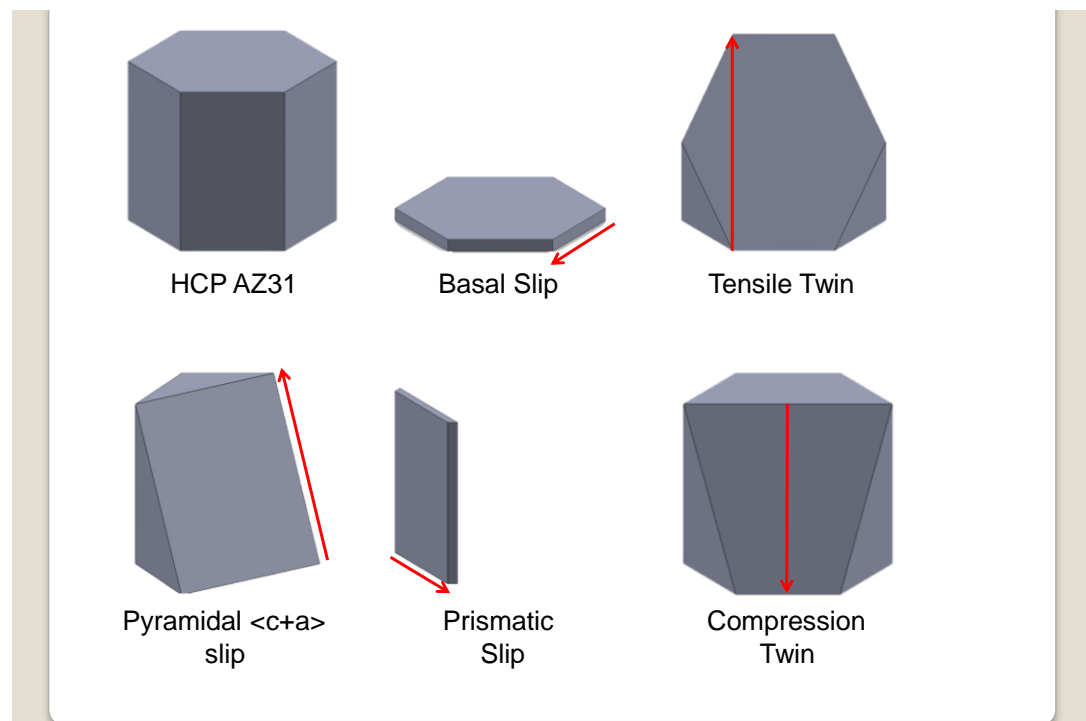
Figure 1. Illustration of planes and directions for five deformation modes in Mg alloy.

9

One contributor to fracture is compression twinning. This can occur during compression along the C-axis or tension perpendicular to it. Acting on the $\{10\overline{1}0\}$ plane, this system reorients the twinned material by 56° and results in shrinkage along the C-axis. For both twin types, the twins are "born" at a lower strain than the surrounding parent material [23]. In compression twins, the reorientation results in a high Schmid factor for basal slip and immediate activation of the same, adding to the strain mismatch. Alternatively, tensile twinning can occur, leading to double-twins and crack initiation [24]. Although difficult to detect due to their typically thin nature, failure and crack initiation is frequently associated with compression twin activity [25]. For instance, Babak and Benzerga found that microcracks observed after interrupted tensile testing in AZ31 followed the direction of compression twins and double-twins[26].

Temperature Dependence of Deformation Mechanisms

Like any other metal, deformation in magnesium alloy requires lower stress with increasing temperature, as average atomic bond length grows and bonds weaken. This does not impact all deformation mechanisms equally, and in fact the impact on deformation characteristics can be dramatic with a shift of 100°C. The most prominent deformation system at room temperature is basal slip due to its low critical resolved shear stress (CRSS) ratio. Table 2 lists the CRSS ratios for some of the systems. These values, from Jain and Agnew [22], are widely used for crystal plasticity modelling of AZ31. As temperature rises, these CRSS values converge, resulting in a relatively isotropic deformation. Combined with changes to defect accumulation, these converging CRSS values serve to enhance ductility at higher temperatures. Jäger and his

10

colleagues demonstrated that rolled AZ31 increased in ductility from 20% at room-temperature to 125% at 300°C [27]. Such high strains in AZ31, and superplastic behavior generally, requires an additional set of behaviors from the material at high temperatures.

Table 2. Critical Resolved Shear Stress ratios for AZ31 [22].

Mechanism	Temperature (^{o}C)	CRSS ratio
Basal Slip	20	1
	150	1
	175	1
	200	1
Prismatic Slip	20	3.2
	150	2
	175	1.9
	200	1.8
Pyramidal <c+a> Slip	20	5
	150	2
	175	1.9
	200	1.8
Tensile Twinning	20	1.5
	150	1.7
	175	1.9
	200	2.1

In addition to the aforementioned slip and twinning systems, there are two other important material behaviors that are typically active at elevated temperatures. First is dynamic recrystallization (DRX). Although the total strain accommodated by grain

boundary movement is low, the effect on microstructure is significant. As discussed by Ponge et al., when DRX occurs in AZ31 and similar alloys, the original grain boundary serves as a nucleation point for many simultaneously appearing grains [28]. These grains form a "necklace" that propagates the further nucleation of additional grains, until, given sufficient energy from strain and temperature, the original grain is consumed by the new, smaller grains. The second important high-temperature mechanism is grain boundary sliding (GBS). This usually accounts for only a few percent strain under the conditions of interest in this study, but given preferable texture, high temperatures, low strain rate, and small grain size can accommodate superplastic strains [29]. Koike et al. found that GBS in rolled and annealed AZ31 contributed significantly to tensile deformation even at room temperature [30]. By observing out-of-plane grain movement after 10% elongation at various temperatures, they estimated that GBS contributed 1% at room temperature and nearly 3% at 250°C. While DRX and GBS mechanisms have little direct contribution to overall strain during severe plastic deformation, they can reorient grains for easy slip, making them important to texture development at elevated temperatures.

CHAPTER II

EQUAL CHANNEL ANGULAR EXTRUSION AS A METHOD FOR

CONTROLLING TEXTURE AND GRAIN SIZE IN MG ALLOY*

Introduction

Equal Channel Angular Extrusion

Equal Channel Angular Extrusion (ECAE) is a severe plastic deformation

technique that has seen widespread use in research facilities beginning in the late 1990s

[31]. Consisting of two intersecting channels as illustrated in Figure 2, the method is

unusual among forming operations in that the workpiece exits the process with

essentially the same dimensions as the incoming piece. This permits repeated processing

with minimal reworking [32] and the ability to reach strain levels in bulk material

previously reserved for wires, sheets, and foils. Maximum shear strain per pass and

highest strain uniformity is achieved when the angle of intersection (indicated by φ in

Figure 2) is 90° and the corners are sharp, as is the case for all tooling in this study.

Rotation about the long axis of the workpiece (extrusion direction) before re-insertion

defines the "route" or strain path. Route A implies no rotation, Route B_c is repeated 90°

rotation, Route C is repeated 180° rotation. Other routes are essentially combinations of

these, such as Route E, wherein rotation alternates between 180° and 90°. These routes

allow the user to select shear planes and directions within the material, a key capability

for processing anisotropic material such as magnesium alloy.
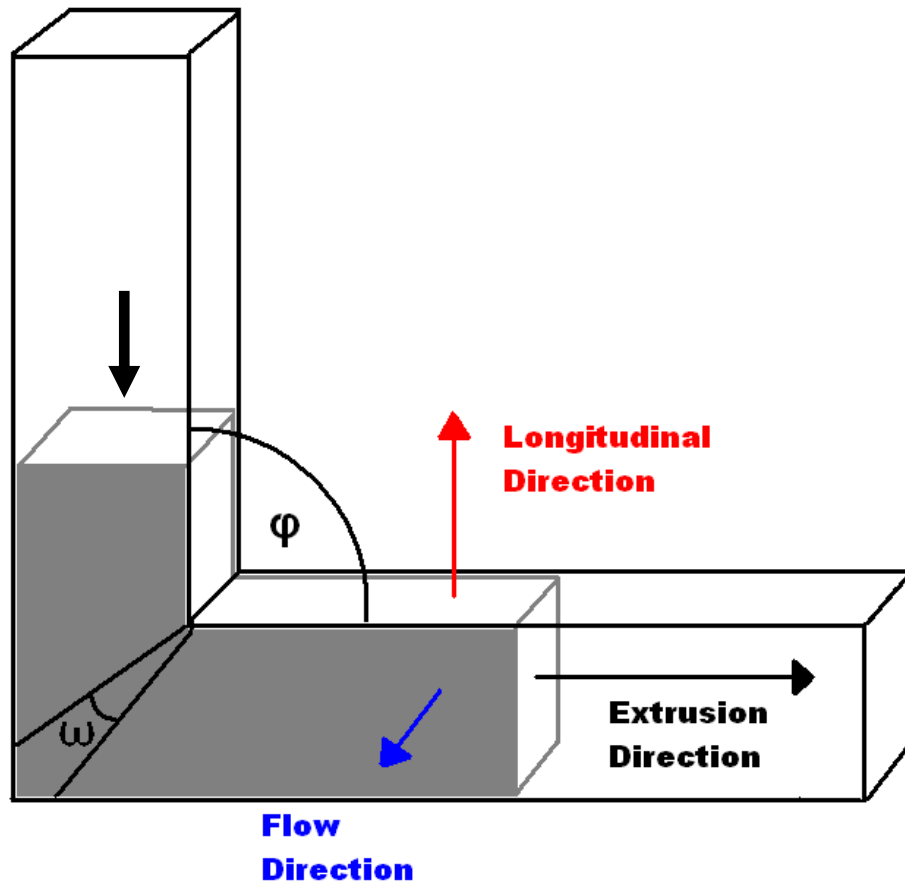
Figure 2. Illustration of ECAE with major orthogonal directions labeled.

A significant additional tooling feature used in this work is the backpressure system. The exit of the workpiece from the channel intersection is restrained by this system, increasing hydrostatic pressure at the intersection. This hydrostatic stress inhibits shear banding and crack formation. Lapovok and her colloeages studied this phenomenon in detail [33-34] but it should be noted that she used fixed-wall tooling. The sliding wall tooling used in this study reduces friction and prevents some of the

phenomenon she and her colleagues observed, such as shear zone thickening. Low friction and elevated hydrostatic stress combine to produce uniform deformation throughout the material.

ECAE has been used to study the effects of severe plastic deformation (SPD) on Mg alloys with the intent of improving mechanical performance [29,35-39]. Several groups have achieved significant increases in strength and ductility in Mg alloys using ECAE [37-39]. The most striking report, by Ding et al. [37], revealed a tensile yield strength of 372 MPa and an ultimate tensile strength of 445 MPa using a multi-temperature hybrid ECAE processing route on AZ31. Unfortunately, they did not present their rationale for choosing specific temperatures and strain paths used to accomplish these strength levels. On the other hand, most reports on ECAE processing of Mg alloys with routes such as A, B_c, and C do not exhibit such high strength levels [37,40]. Some processing conditions have been reported to result in even lower post-processing strength and/or ductility as compared to the starting commercial material [37,40,41], in spite of the microstructural refinement. These reported performance drops are often related to higher processing temperatures (200-300°C) which encourages dynamic recrystallization and softening, and sometimes to failure to take the effect of crystallographic texture into consideration on the mechanical response of Mg alloys. The direction of loading with respect to the ECAE processing induced textures can explain the drop in strength observed in uniaxial mechanical testing, due to the large anisotropy in the critical resolved shear stresses of deformation mechanisms in Mg alloys {42-44}. Unfortunately, with few exceptions [44,45], the literature presents only unidirectional

15

testing of the starting and deformed materials, and in some cases presents no texture data at all. Biswas et al. present a comprehensive study in which they are able to ECAE process crack-free pure Mg at room temperature via route A, but do not report mechanical properties [42].

Some of the material in this study underwent processing similar to the study by Ding et al. [37] and Biswas et al. [42]. Ding et al. report that extrusions were carried out in a 120° angle ECAE tool at several temperatures, starting with 200^oC and ending at 115^oC. Biswas et al. extruded their material in a 90° ECAE tool with the first four route A passes being performed at 250^oC, followed by a progressive scale down of temperature, with the eighth pass being performed at room temperature. The ECAE group at Texas A&M has previously used a similar temperature step-down method to SPD process difficult-to-work materials and others have also used a multi-temperature approach in Mg alloys [41]. The temperature step-down method results in an incremental grain refinement by both dynamic recrystallization (DRX) at higher temperatures [42], [46] and conventional defect accumulation throughout the temperature range [42]. This method allows for uniform grain refinement at higher temperatures with the help of DRX. Lower temperature processing benefits from more involvement of grain boundary mediated mechanisms in deformation, suppressing the shear localization or cracking that often occurs in Mg alloys processed at a single low temperature. The stepping down of temperature is key to successfully taking advantage of the grain refinement available at lower temperatures.

Plate ECAE

Given the plate form of several targeted applications, it was important to demonstrate that ECAE could enhance plate AZ31 in a manner similar to bar forms. Very little exists in the literature concerning plate processing. This is likely in part due to the increased press loads and more buckling-prone punch geometry (per cross-sectional area) than square or round bars when using the fixed-wall tooling common to university research labs. However, processing of soft materials like pure aluminum [47] or hot Mg alloy (300°C on a Mg-0.6% Zr alloy) [48] has previously been demonstrated in this type of plate tooling. More relevant to the tooling in this study is the plate tooling at Honeywell, designed by the inventor of the ECAE process, V.M. Segal. Again, publications focus on aluminum, but the sliding floor in this tool reduces friction and increases uniformity [49]. One key difference between plate and bar processing is the 90° rotation in B and B_c routes. In the case of bar, this rotation is around the long axis, while in plate it is about the plate normal. As noted by Furukawa et al [50], the B_c strain path still returns an ideal element back to its original form every four passes. However, the angle between prior shear planes and the shear plant of each new pass differs. As will be shown in this chapter, this difference leads to a change in texture when processing Mg alloy.

Materials and Methods

The majority of the material used in this chapter is AZ31B hot-rolled plate. This is nominally a single-phase 3%Al, 1%Zn magnesium alloy, although particles and impurities do exist and vary based on supplier. The grain size can also vary, due in part to total strain and rolling temperature. The bar processing discussed in this chapter began with a 25mm thick plate, while the plate processing began with a 13mm thick plate. A more thorough description of this starting material leads the next section. Two additional alloys, ZK60 and WE43, are also discussed. The ZK60 was an extruded material nominally consisting of 6% Zn and 1% Zr and with a bimodal grain size. The WE43 was a rolled plate nominally consisting of 4% Y and 3% rare earths (primarily Nd and Gd based on our measurements). Finally, our first processing, discussed in the "problems" chapter, utilized cast AZ31 and ZK60.

ECAE processing utilized an MTS press with custom dies designed by Robert Barber. Bar processing was conducted using a die with 25mm x 25mm channels intersecting at a sharp 90° angle that was heated externally. For the fabrication of the bars processed only at 200°C, the plate was sectioned to 25 mm $\times$ 25 mm $\times$ 150 mm bars and lubricated before extrusion. The material for the bars designated with an H was sectioned to 19 mm $\times$ 19 mm $\times$ 125 mm and encapsulated in an interstitial-free steel square tube (with external dimensions of the larger bars) in order to facilitate the application of large backpressure loads in the die. The plate processing utilized bare pieces that were 15.25cm x 15.25cm x 1.25cm in dimension to match the tool channel cross section. The tool was heated with uniformly dispersed cartridge heaters in close

proximity to the channels. Finally, one case will be discussed wherein alloy WE43 was extruded utilizing an isothermal die at temperatures in excess of 500°C. This die is heated externally and enclosed in an argon environment. Bars for this processing were 19mm x 19mm x 125mm in size. Finally, the initial processing on cast material described in the "problems" section was performed using 13mm diameter x 60mm length rod pairs encapsulated in 25 mm × 25 mm × 150 mm bars.

Optical and secondary electron micrographs (SEM) were prepared using a picral etch after mechanical polishing. Transmission electron micrographs (TEM) were prepared from 3 mm discs, ground to 100 μm then thinned using a twin-jet polisher with a 5% HClO$_4$/methanol solution. Texture measurements through X-ray diffraction were performed using a Bruker AXS D8 Discover diffractometer with a Cu-K$_\alpha$ source operating at 40 kV and 40 mA. Mechanical testing was performed using 4mm x 4mm x 8mm compression samples and dogbone tension samples with an 8mm long gauge section of 1.5mm thickness and 3mm width. Samples were tested at room temperature at a strain rate of 5 x 10^{-4} s^{-1}. All of these samples were initially sectioned using wire electrical discharge machining. They were removed only from fully-processed material, as opposed to the end regions of the ECAE processed workpiece that did not undergo shear during every extrusion of the series.

Results and Discussion

Characterization of Starting Material

The starting plate is typical of AZ31 hot rolled material, but a characterization is useful for its comparison to the ECAE processed materials. The texture, microstructure, and mechanical response are depicted in Figure 3. The texture that developed has the basal planes primarily aligned within 10 degrees of parallel to the plate surface and the prismatic planes have a weak alignment with the long transverse direction. The arrangement makes sense when observing the deformation planes and directions in Figure 1 if one were to think of rolling in simplistic terms. Consider that rolling is a slightly obfuscated compression in the plate normal direction and extension in the rolling direction. The basal, prismatic, and pyramidal slip would all tend to align the prismatic planes with the long transverse (the center of the $(10\bar{1}0)$ pole figure) and the highly active basal slip in conjunction with pyramidal slip would align the basal planes with the plate itself. The microstructure consists of equiaxed DRX grains typical of large deformations at high temperatures. In this case, average grain size is 25 μm and the typical range is 10-70 μm. The mechanical response is depicted in two directions as the normal direction (ND) and rolling direction (RD). While the long-transverse properties are not depicted, they are almost the same as the RD. Notice that the tension response in one direction is quite similar to the compression response in the other. These responses are typical of the dominant room temperature mechanisms, basal slip and tensile twinning.
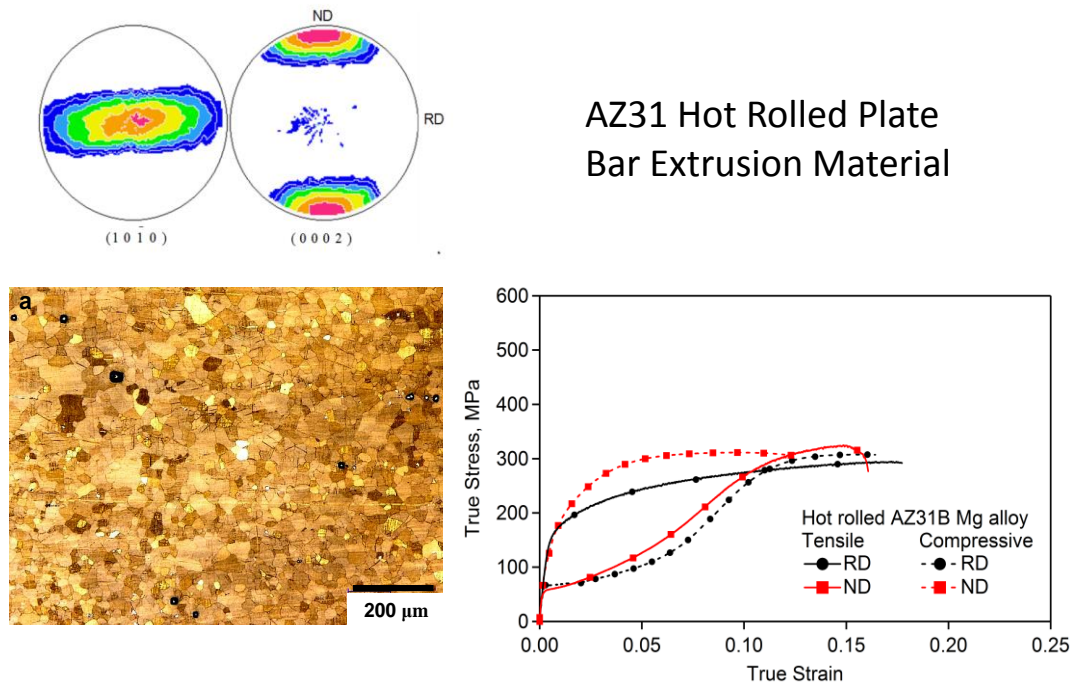
Figure 3. Microstructure, prismatic and basal pole figures, and mechanical response of AZ31 hot-rolled plate.

The starting material for the AZ31 plate extrusions was similar to the bar starting material, with a somewhat wider grain size distribution and larger (28 µm) average grain size. The mechanical anisotropy is slightly lower than the other plate as shown in Figure 4. We do not expect these differences to significantly impact the properties of ECAE-processed plate as compared to the bar material.

AZ31 Hot Rolled Plate
Plate Extrusion Material
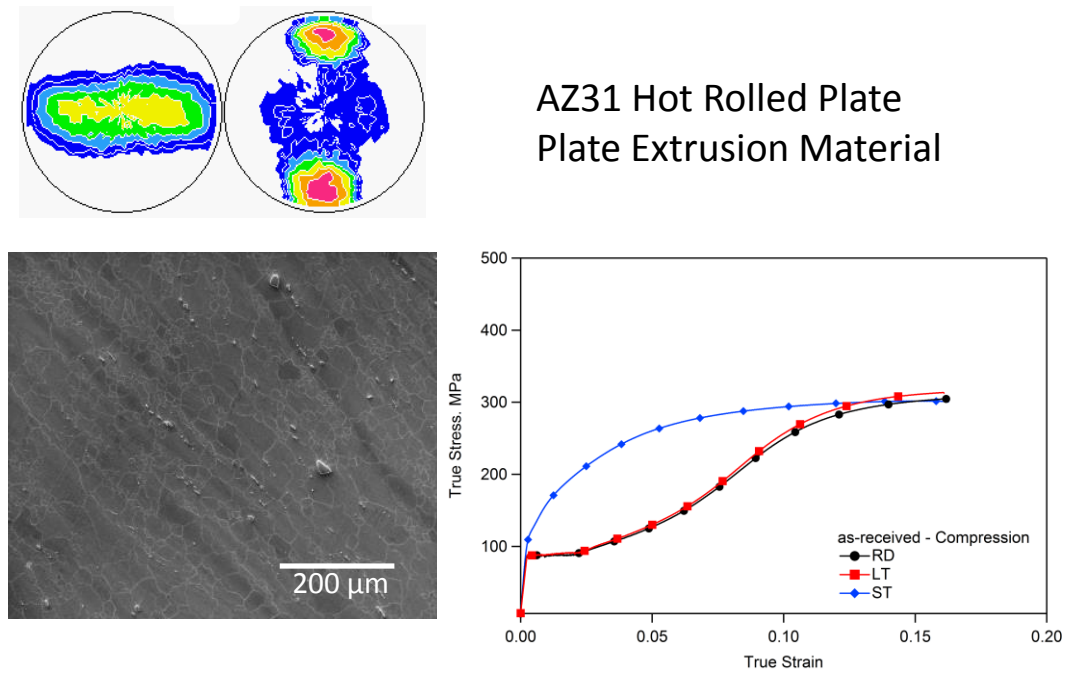
Figure 4. Microstructure, texture, and mechanical response of AZ31 hot-rolled plate used for plate processing.

The ZK60 material shown in Figure 5 appears at first to be a cast material due to the large grains surrounded by a sea of finer grains. Indeed, the slight difference in color between the populations in the optical micrograph are revealed to be chemical segregation in the accompanying back scattered electron micrograph and matching WDS chemical map. The large grains are Zn and Zr enriched, indicating that the material was not cooled rapidly during casting. Despite the appearance of a cast material, the basal texture accompanying Figure 5 has a classic round extrusion character. Some additional comments on the alloy will be made in the "Problems" section.
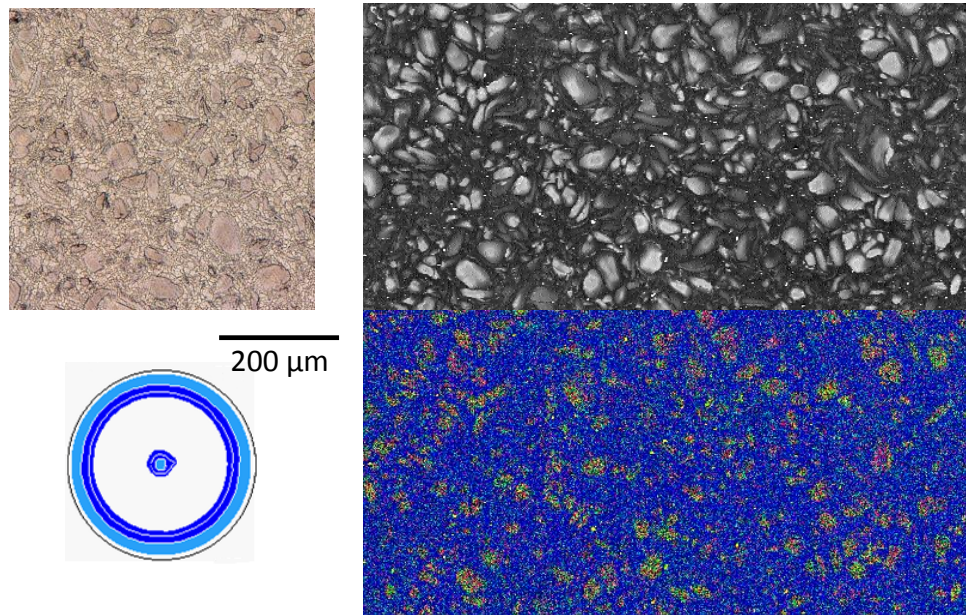
Figure 5. Optical and backscattered electron micrographs, basal texture, and WDS chemistry map of ZK60A from Timminco.

ECAE Route Development and Grain Refinement

In order to develop a baseline for its behavior while undergoing ECAE, we extruded AZ31 bars for one, two, and four passes at 200°C. The breakdown of microstructure during the initial extrusion leaves some regions refined while large undeformed grains remain, as pictured in Figure 6. The process is that of necklace type dynamic recrystallization as described in the introduction to this chapter. These large grains are reduced in size and number after the second pass, and by the fourth pass the microstructure consists almost entirely of the DRX grains.
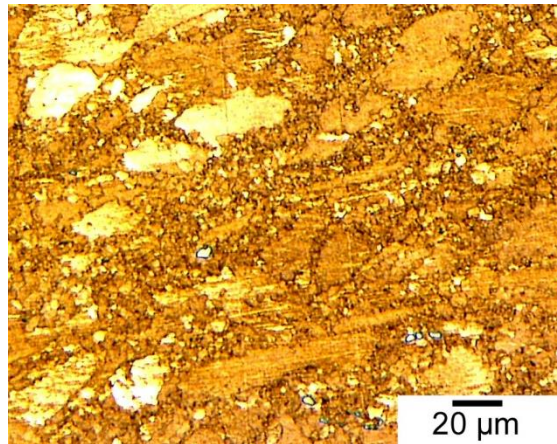
Figure 6. Optical micrograph of AZ31 processed 1A at 200°C.

The average grain size in the four-pass material depends, to a small extent, on the processing route. Figure 7 contains optical micrographs and basal pole figures after 4A, 4C, 4E, and $4B_c$ processing. The 4A and 4C materials average close to 4 μm while the $4B_c$ is the most refined, averaging 3 μm. My colleague Majid Al-Maharbi worked with a visco-plastic self-consistent crystal plasticity model in order to aid our understanding of the difference in grain refinement level between routes [43]. In addition, he performed additional extrusions wherein the workpiece was first inserted with the long-transverse direction of the plate parallel to the exit channel, rather than the plate normal parallel to the exit channel as in all of the bars processed for this work. This experiment revealed that the alternate starting orientation suppressed DRX and primarily deformed the grains in a conventional manner. Coupled with the predictive modeling, he postulated that the non-basal slip activity, which was predicted to be much higher in the alternate orientation, lead to this suppression of DRX. Barnett found that DRX was lowest in

24

conventional compression samples when prismatic slip was most active [51]. This activation of non-basal slip lowers the energy available for the DRX process. The VPSC model was also used to predict slip system activity using conventional ECAE routes. After four passes it is the routes that rely more on non-basal slip, $4B_c$ and 4E, that are most heavily refined. The initial microstructural breakdown during the first two passes was more efficient using DRX to quickly convert material to fine grains. However, these DRX grains are a 1-5 μm population that does not shrink upon repeated deformation. When prismatic slip is heavily activated, as in the B_c route, DRX is a secondary mechanism and conventional grain refinement can take place in the final extrusions. This leads to the slightly lower average grain size, but DRX is not completely suppressed and the dislocation recovery at 200°C prevents further refinement by cell structure formation. Our approach to solving this issue and refining by another order of magnitude will be covered in this section, but first the crystallographic texture generated by these conventional routes will be discussed.
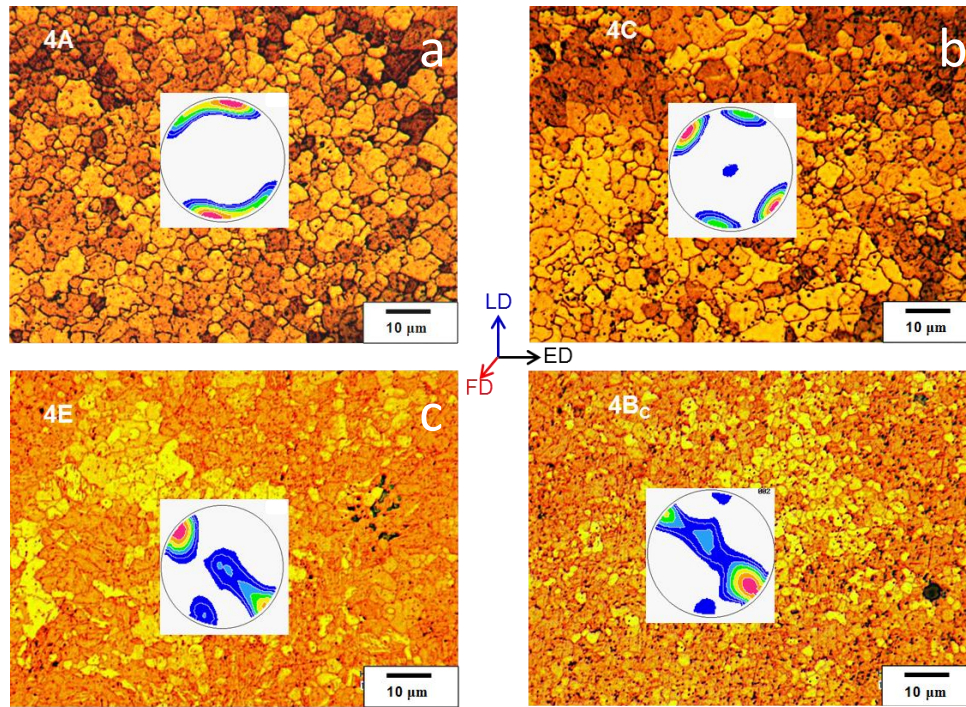
Figure 7. Micostructures and textures of AZ31B after four-pass 200°C ECAE processing via routes (a) A, (b) C, (c) E, (d) B_c.

The four basal textures in Figure 7 are indicative of the shear orientations and respective deformation mechanisms activated during processing. We refer to these as A-type, C-type, and spread textures. The 4A texture is, in this case, slightly more spread than the ideal A-type but still closely resembles the rolled plate texture with basal poles primarily oriented along the longitudinal direction (LD). In the case of the ECAE processed bars, the LD is analogous to the plate ND. The 4C texture is again a weaker version of the ideal C-type, which would consist of basal poles aligned 45° from LD and ED. The spread textures are strongest at this same point, but are much more diffuse in alternate orientations. These textures form due to the tendency for the active slip planes

to align with the shear plane of the ECAE processed bar. In the 4C case, shear is cyclically applied, returning the deformed sub element to its original shape every two passes. After a strain of nearly five, the basal planes, on which slip is easiest, have aligned with the shear plane. While the bar is not rotated during the 4A case, the prior shear planes are actually rotating continually towards alignment with the extrusion direction as the deformed sub elements are stretched out along this direction. This leads to the activation of non-basal slip, as the VPSC modeling revealed, and maintains most of the basal poles parallel to the longitudinal direction. The $4B_c$ material has undergone repeated 90° reorientations, requiring even more non-basal slip than the 4A case. Many grains are not able to realign the easiest slip plane with the shear plane during each pass, so the basal texture is "spread" between prior orientations and the last shear plane. While temperature affects the relative activity of different deformation systems, the basis for the formation of these textures remains the same for the other ECAE processing discussed in this work.

The room temperature mechanical properties of the four-pass materials are depicted in Figure 8. One of the most obvious correlations with the textures in Figure 7 is the inverse relationship between spread in yield strength and spread in texture orientation. As indicated by the CRSS ratios in Table 2, basal slip and tensile twinning are much easier than prismatic or pyramidal <c+a> slip at this temperature. Taking 4C as an example, the four curves with low yield strengths are compression and tension in the extrusion and longitudinal directions. In all four cases, the bulk of the basal planes are at a nearly 45° angle to the loading axis, so basal slip is easily activated. The hardening

observed here is primarily an effect of the rotation of basal poles towards the load axis, increasing the applied stress required to continue slip. The flow direction of 4C illustrates the two other major deformation mechanisms. The FD compression sample has a plateau after yield, followed by rapid hardening. This is a classic tensile twinning response. Although this data is from compression testing, the C axis extends as the A axis is compressed. Since the FD loading places most basal poles 90° from the load axis, basal slip is unavailable due to near-zero Schmid factor. Since extension twinning has a lower CRSS than the non-basal slip mechanisms, tensile twinning takes place. In the FD tension case, on the other hand, it is the A axis that is extending in most grains and the C axis is contracted. Since tensile twinning is unidirectional, pyramidal <c+a> is the only mechanism available to accommodate plastic deformation in the C axis for most of the grains. The primary active slip system is prismatic slip, since it has a much lower CRSS than pyramidal <c+a>. Thus, the FD tension case has the highest yield strength because the two easy deformation modes are not available. Although the underpinnings of this deformation behavior are further examined in Chapter III, VPSC modeling was quite useful in developing our initial understanding of the mechanical behavior. Readers interested in further reading on this matter are referred to Al-Marahbi's knowledge base, on which he continues to expand [43,52,53].
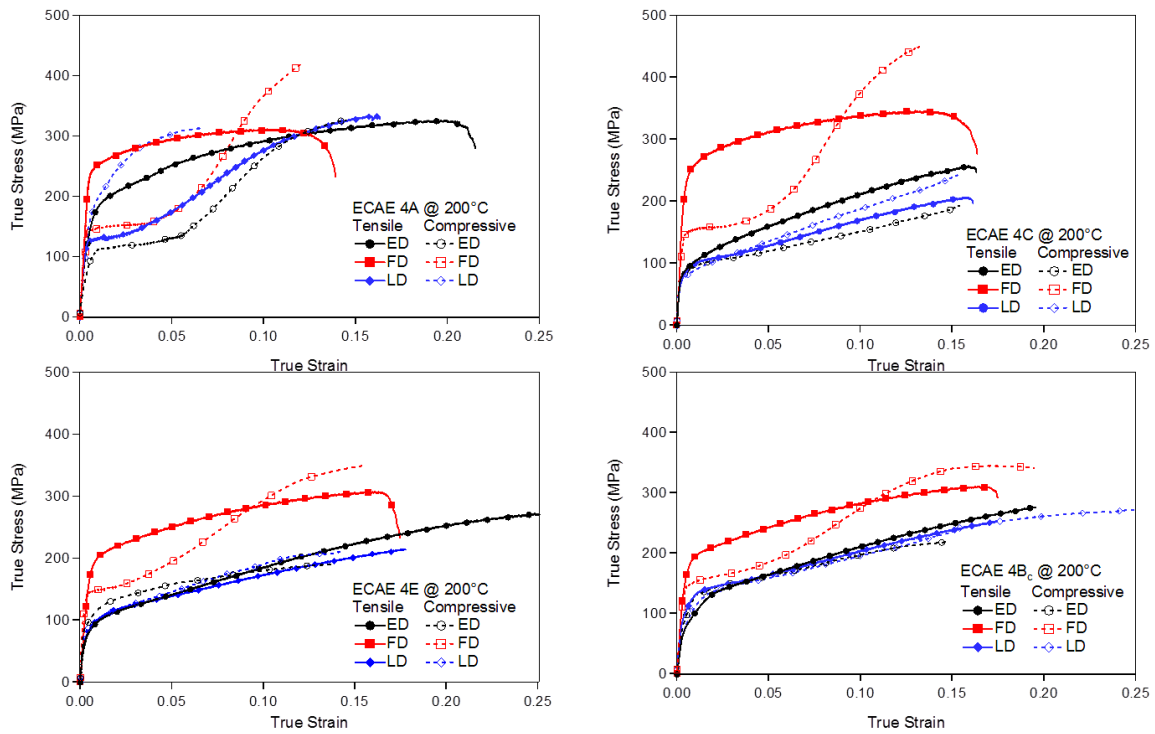
Figure 8. Mechanical responses of AZ31B after four-pass 200°C ECAE processing via four routes.

Based on our initial results, VPSC modeling, and knowledge of changing deformation behavior with temperature, we designed routes that would allow us to refine the microstructure to ultra-fine-grain (UFG) levels and provide some control over texture. We discovered early on, however, that low-temperature route B_c processing would be difficult at best. As shown in Table 1, the CRSS ratios of non-basal slip increase and tensile twinning becomes easier as temperatures drop below 200°C. This results in heavy twin activity during extrusion after 90° rotations. As will be discussed in Chapter III, the strain mismatch between twin and parent can lead to failure, and we observed shear banding and cracking in the billets where such low-temperature Route B_c

was attempted. With no clear path forward to a "spread" texture UFG material, we focused on generating A and C type textures. The two most successful, which we repeatedly created for several experiments, are referred to as 5H and 7H. The strain paths, depicted in Figure 9, are designed to take advantage of DRX for initial refinement followed by conventional grain refinement through dislocation accumulation.

5H   **7H**

2A @ 200°C ⟵ DRX ⟶ 4A @ 200°C
Initial breakdown of microstructure

1C @ 150°C ⟵ Basal Slip ⟶ 1C @ 150°C
Suppress shear localization

1A @ 150°C ⟵ Basal + Nonbasal ⟶ 1A @ 150°C
Harden slip systems

1C @ 125°C ⟵ Basal   Mixed ⟶ 1A @ 125°C
Generate final texture, grain refinement
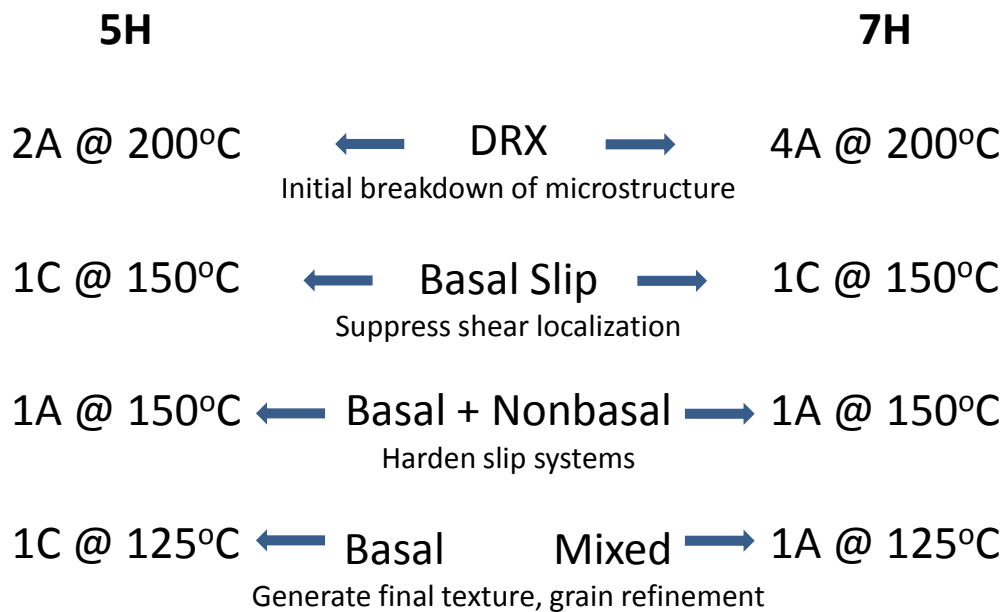
Figure 9. Depiction of ECAE routes and temperatures for hybrid processing of 5H and 7H AZ31 material.

The two routes are designed to generate a uniform, fine microstructure. In both cases, route A is used at 200°C to heavily activate DRX and to avoid shear localization that the repeated shear of Route C can encourage. The first low temperature pass in both cases is a C pass at 150°C, intended to promote basal slip and suppress twinning. This is

followed by an A pass, intended to take advantage of both basal and non-basal slip. In the last pass, temperature is lowered to 125°C but the route choices differ. In 5H, the C route promotes a C-type texture while the A route in 7H promotes an A type texture. While these textures are the primary difference between the routes, the grain sizes also vary. The four initial extrusions in the 7H case ensures that the DRX process had completed before the low temperature extrusions begin. After only two extrusions at 200°C, large grains remained in the 5H material, and thus the grain size was ~0.5µm rather than the ~0.3µm grain size of the 7H case. Optical micrographs of the two materials are in Figure 10 along with the crystallographic textures.
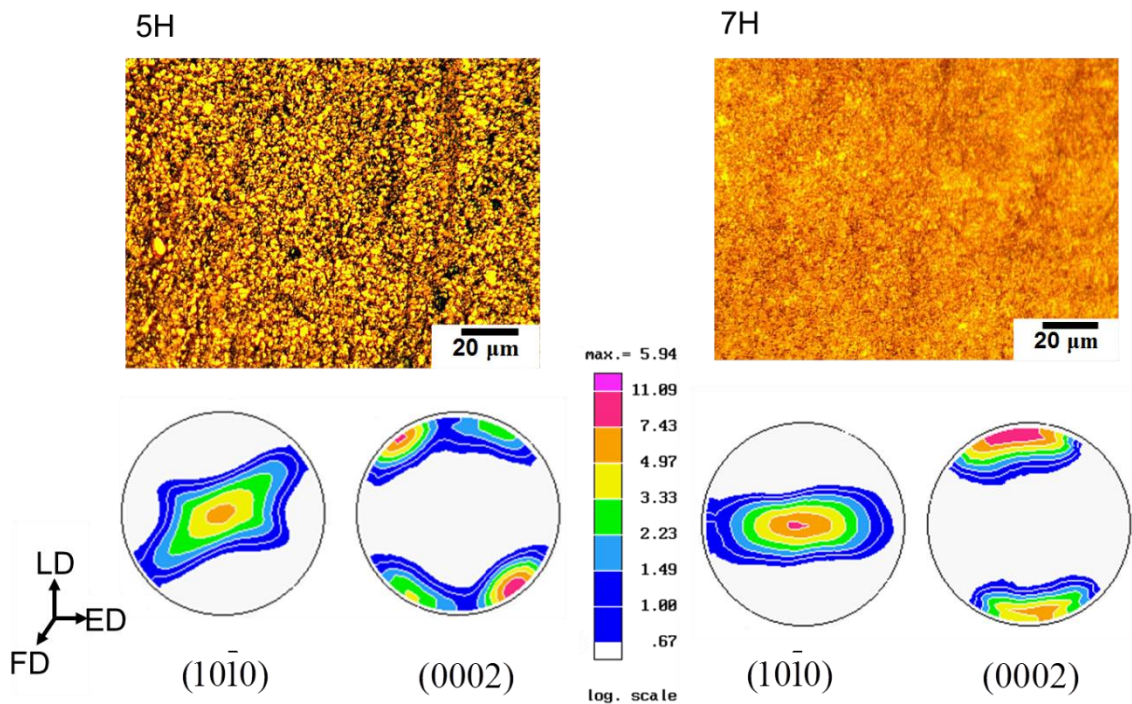
Figure 10. Optical micrographs and pole figure textures of 5H and 7H hybrid route processed AZ31.

31

The C-type and A-type textures here are similar to the 4C and 4A textures in Figure 7. This leads to similar anisotropic mechanical behavior, although our ability to study this was limited to compression testing due to the reduced bar size required by canning in IF steel. Figure 11 depicts the mechanical response of the 5H alloy, along with that of the starting plate material for reference. As compared to the 4C material, one additional test is depicted wherein compression samples were cut with their axis parallel to the basal pole peak. In most grains, this orientation prevents the activation of basal and prismatic slip as well as tensile twinning. This leaves the compression twinning and the difficult to activate pyramidal <c+a> slip. As discussed in the introduction, compression twinning (and associated double-twinning) promotes cracking and failure, so it is no surprise that the material exhibits no ductility in this direction. In other loading conditions, however, the 5H material is clearly dramatically stronger than the starting material.

From the textures, there are two roughly comparable cases between the two materials. First, the compression responses along the FD direction in the 5H sample and along the IP direction in the starting material both show the characteristic of twinning-dominated deformation: a low or no-hardening plateau region in the first stage followed by an upward stress-strain curve in the second stage. The yield strength in this deformation mode responds dramatically to grain refinement, as the 5H sample yields

along the FD direction at almost four times the strength level and ultimate strength goes

to over 500MPa compared to nearly 300MPa for the IP direction of the rolled plate.

Although the deformation hardening is explained by tensile twinning expected in this

type of loading [54], higher yield strength in the FD direction of the 5H sample is at

least partially attributed to the Hall-Petch effect. The second set of readily comparable

samples is the REF compressed along the TT direction vs. 5H material compressed

along the direction called 37°, as both are parallel to a strong basal pole peak. While the

5H material failed immediately after yield, the impact of grain size (and to some extent

the texture) on that yield strength is dramatic. A more careful examination of these

effects is in Chapter III.
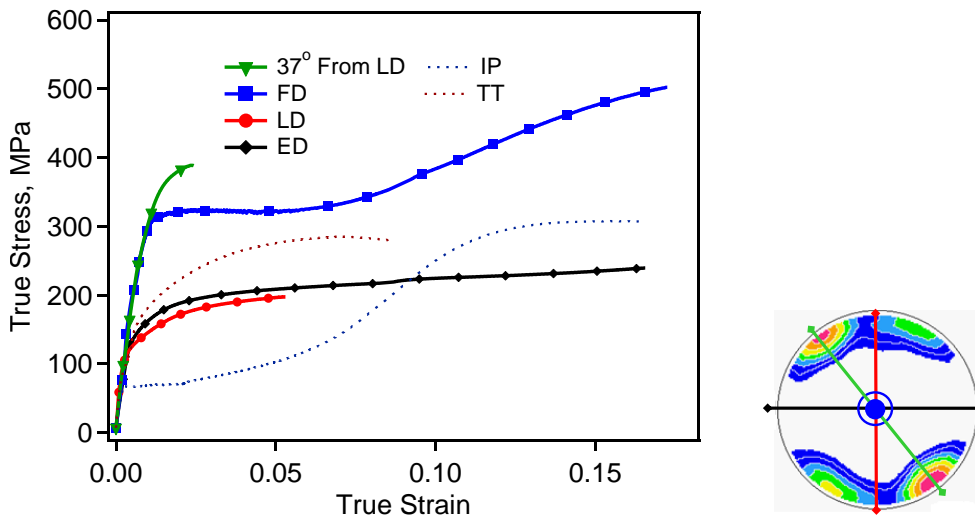
Figure 11. Compressive stress strain response of AZ31 in the hot-rolled samples along two directions and for the ECAE processed 5H samples along four directions. 37°: sample in the direction of strongest basal pole intensity, FD: Flow direction, LD: Longitudinal direction, ED: Extrusion direction, IP: In-Plane direction of the plate TT: Through-Thickness direction of the plate. Basal pole figure for 5H included for reference.

The mechanical response of the 7H material and its basal texture are depicted in Figure 12. While the FD response is similar to 5H, the other directions exhibit brittle failure. This is related to the shear banding that we observed in the material, both indicating that Route A is problematic at 125°C. As indicated by the CRSS trends in Table I, non-basal slip requires a relatively high stress to activate once temperatures fall to this level. Although Route A is not impossible at this temperature, this requires that the material has a C-type texture prior to the final A pass, and the resulting texture is a spread between A-type and C-type [55] due to the greater availability of basal slip compared to repeated route A extrusions.
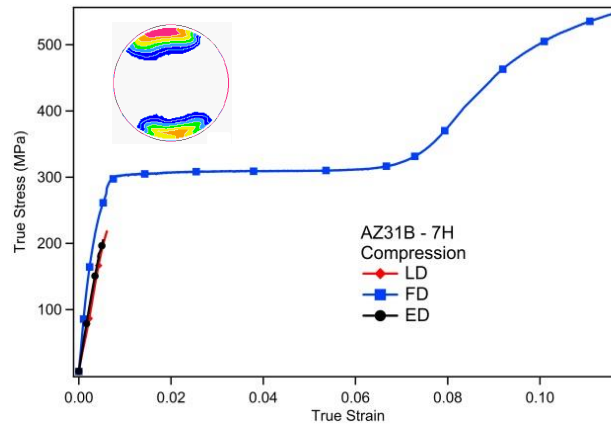
Figure 12. Compressive stress strain response and basal pole figure of AZ31 processed 7H.

A comparison can be made between several materials of A-type and C-type textures. Figure 13 is a comparison of mechanical response in the FD direction under tension and compression for several materials. In both types, the tension response from the hybrid materials is not present due to size restrictions imposed by canning. The

compression results, however, indicate the dramatic impact on twinning. While we

initially hoped that this would lead to reduced tension-compression asymmetry through

grain refinement, the grain size sensitivity of prismatic slip is at least as significant. This

subject is covered at some depth by Al-Maharbi and by Razavi [53,55-57].
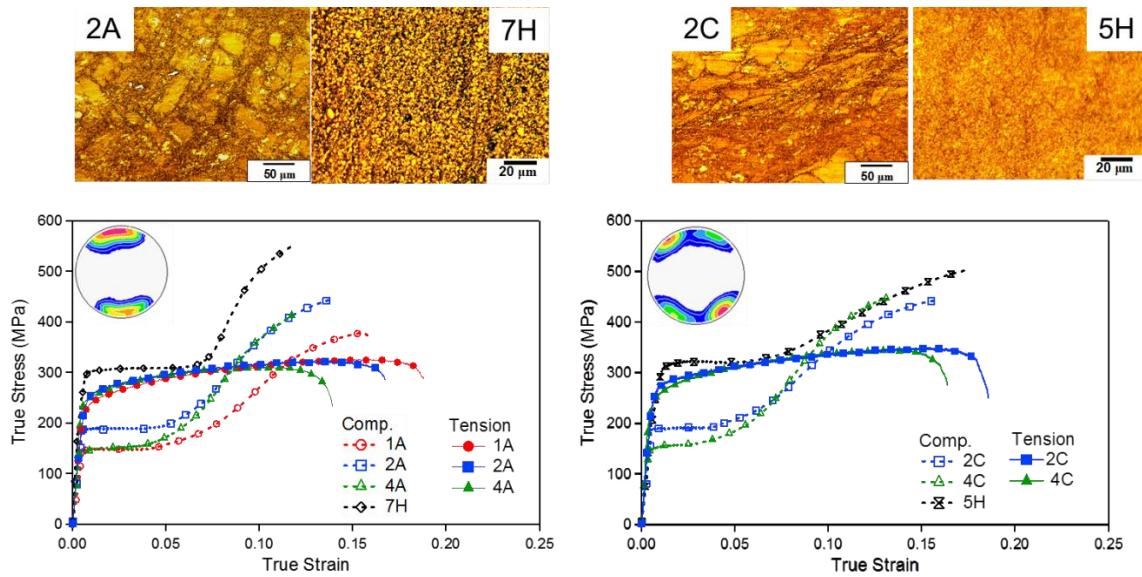
Figure 13. Microstructure and mechanical response in the flow direction of ECAE processed materials with two texture types.

Although it is not the focus of this work, ZK60 provides some perspective on the

processability and achievable properties of Mg alloys beyond AZ31. The ZK60 material

was processed via hybrid routes in order to grain refine the material and take advantage

of the increased number of active slip systems at low temperatures. The 6% Zn

concentration makes non-basal slip easier to activate while also increasing overall

strength. This increased non-basal slip activity also leads to weakened ECAE textures

and reduced anisotropy in room temperature mechanical testing. Figure 14 is the mechanical response and basal texture of ZK60 processed through eight passes: 2A at 200°C, followed by 1C+1A+1C+1A at 150°C. This strain path results in a spread texture with a large population of poles aligned with the LD (as in A-type texture) but also a significant population aligned with FD and a small C-type component. This spread texture highlights the multitude of deformation processes at 150°C in this alloy. Similarly to the room temperature response of AZ31 with spread texture, the mechanical anisotropy in this case is modest, and ultimate strengths are quite similar.
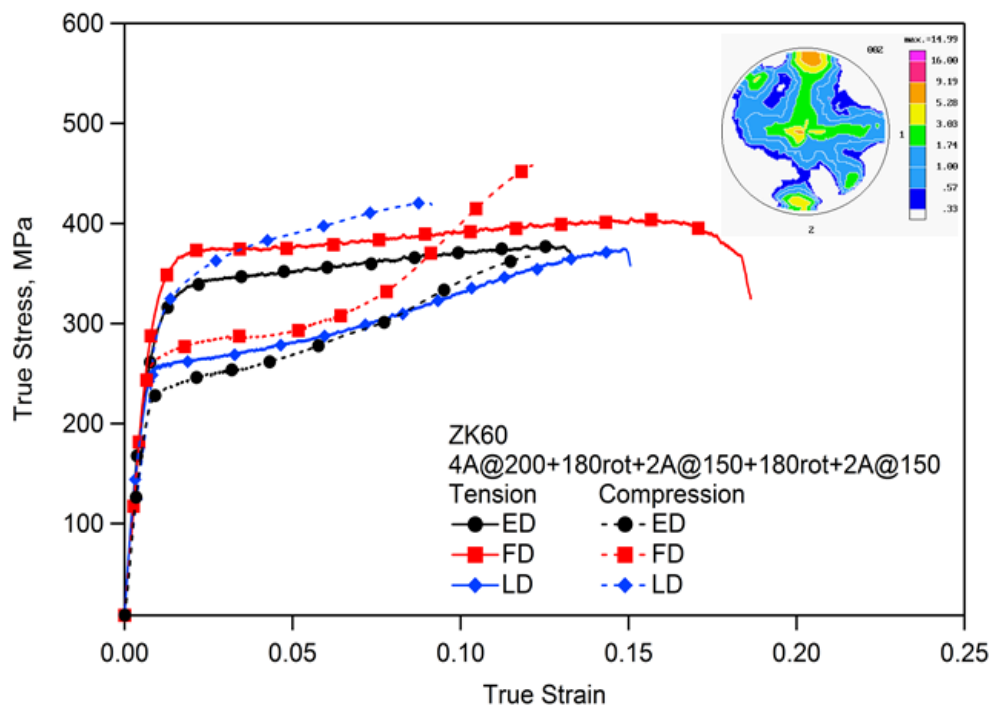
Figure 14. The effect of ECAE processing via 2A at 200°C, followed by 1C+1A+1C+1A at 150°C on ZK60 mechanical properties with pole figure included.

When attempting to refine the microstructure of ZK60 in a small number of passes, the condition of the starting material becomes significant. Figure 15 is the mechanical response, texture, and microstructure of ZK60 after processing 2A at 200°C + 1C at 150°C + 1A at 150°C. The texture is in some ways a stronger version of the eight pass material in Figure 14; the peak intensity is close to LD with a secondary peak at FD. While mechanical performance is significantly improved compared with the as-received material, large grains remain. This inhibited grain refinement will be discussed further near the end of this chapter. Despite the large grains, mechanical response under twinning conditions is excellent, and while ductility during slip is greatly reduced, the yield strength is doubled. This comparison is somewhat confounded by differences in texture but nevertheless illustrates how ECAE processing at 200°C and 150°C can efficiently produce a high strength, low anisotropy magnesium material using ZK60.
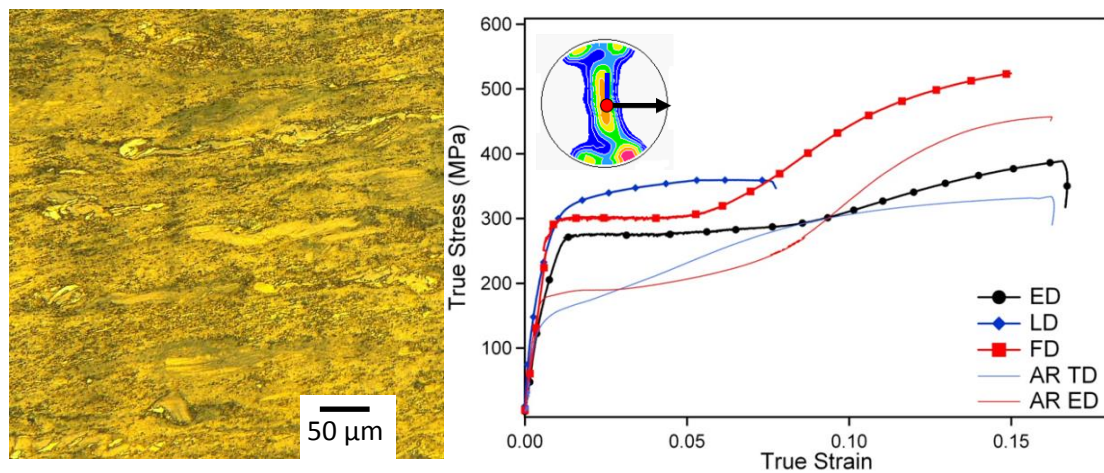
Figure 15. Compression test results, pole figure with directions of mechanical testing indicated, and optical micrograph of ZK60 processed 2A@200°C + 1C@150°C + 1A@ 150°C.

Plate ECAE

One notable difference between the plate and bar extrusions is the absence of backpressure. This absence leads to non-uniform shear and rounded outer corners during the first plate extrusion, as depicted in Figure 16. This phenomenon is reduced in subsequent extrusions but the absense of backpressure limited our extrusions to $150^{\circ}C$ and warmer. Nevertheless, we were able to validate our processing methodology in plate form, as the following results will show.
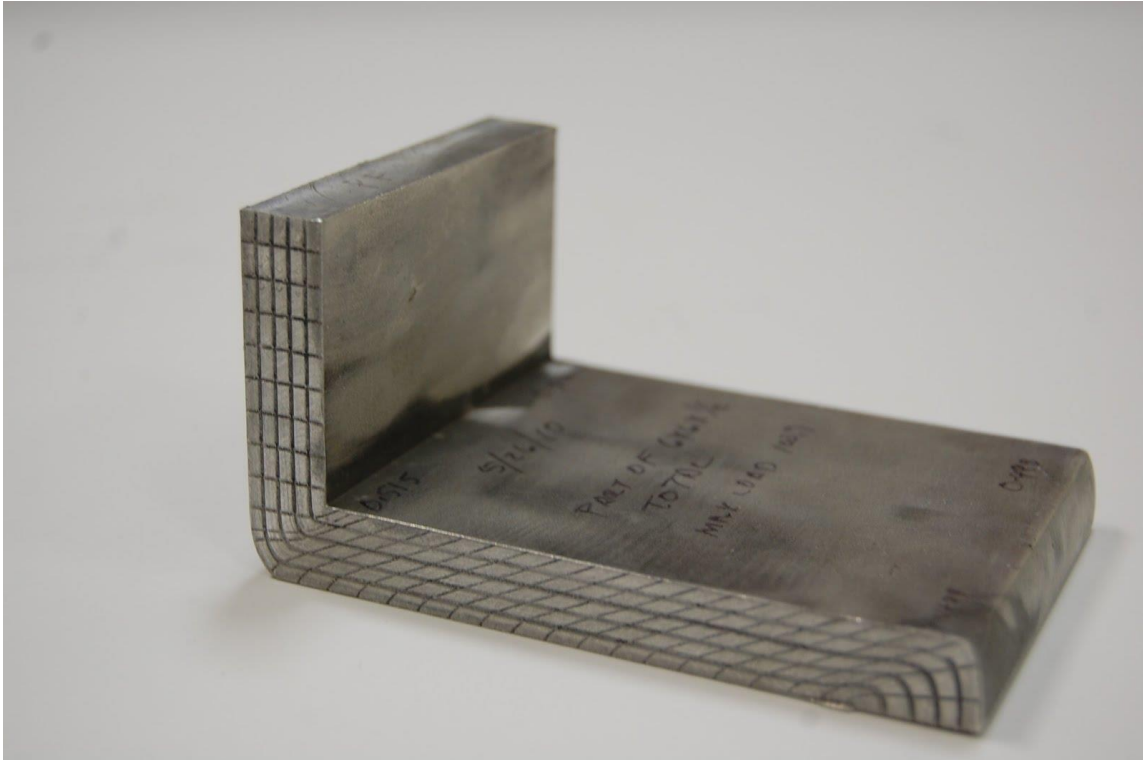
Figure 16. Image of partially extruded plate to which a grid pattern was applied prior to extrusion.

We set out to first show that we could replicate simple bar processing results in plate. Route A and Route C have the same mechanics in plate and bar, so the absence of backpressure should be the only significant factor. Since backpressure is not required to prevent cracking or failure when processing AZ31 at 200°C, we expected, and for the most part achieved, similar results. Figure 17 compares the texture and mechanical properties of bar and plate processed 4A@200°C. The plate texture is closer to a rolling texture than our reference 4A bar, but the peak intensity location and mechanical responses are quite similar. The minor differences are more likely to be the impact of impurities and other possible variations in the starting material than any change in the stress state or shear path due to differing geometries. This falls in line with our expectations based on experience and prior studies [58]. The microstructure of the plate, pictured in Figure 18, is also similar to the bar case, with an average grain size on the order of 5 μm.
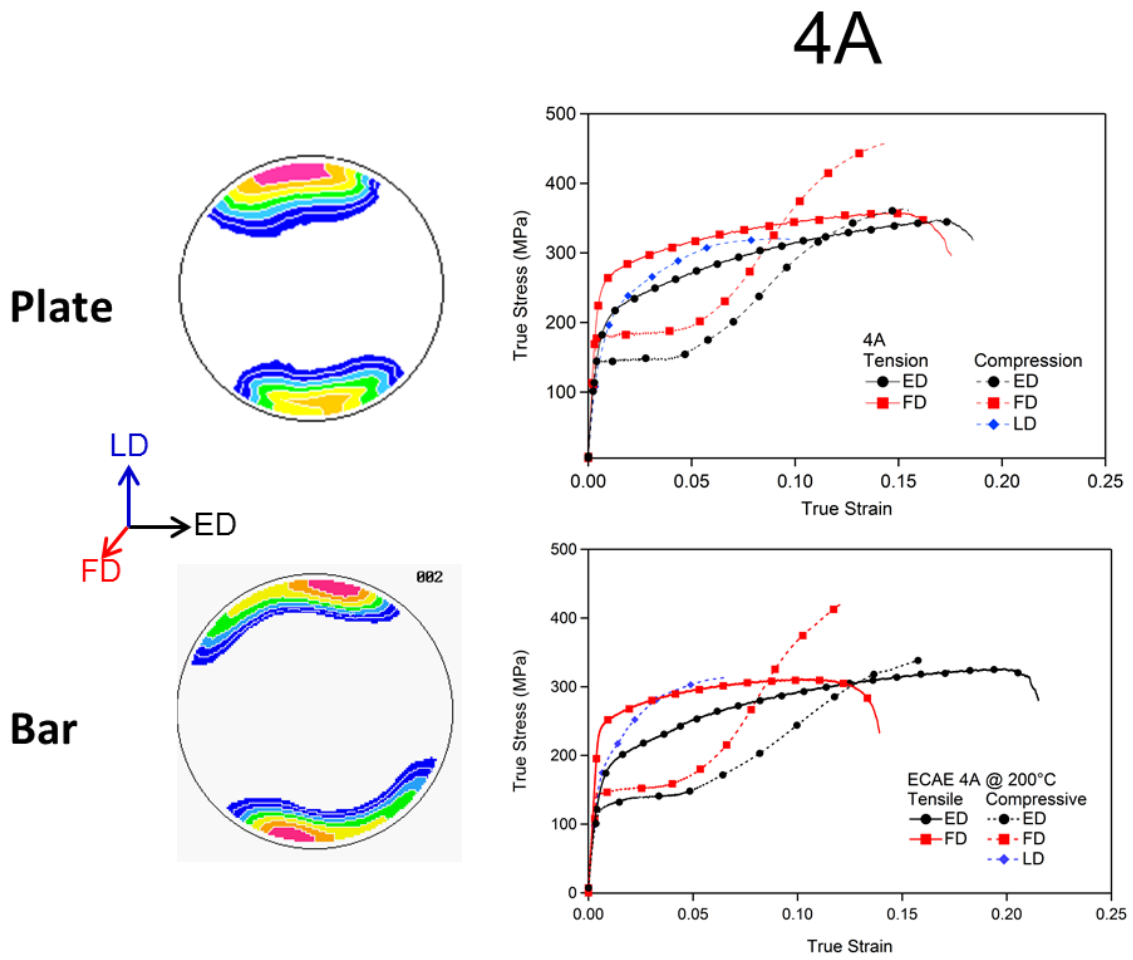
Figure 17. Comparison of basal pole figures and mechanical responses of AZ31 processed 4A at 200°C.
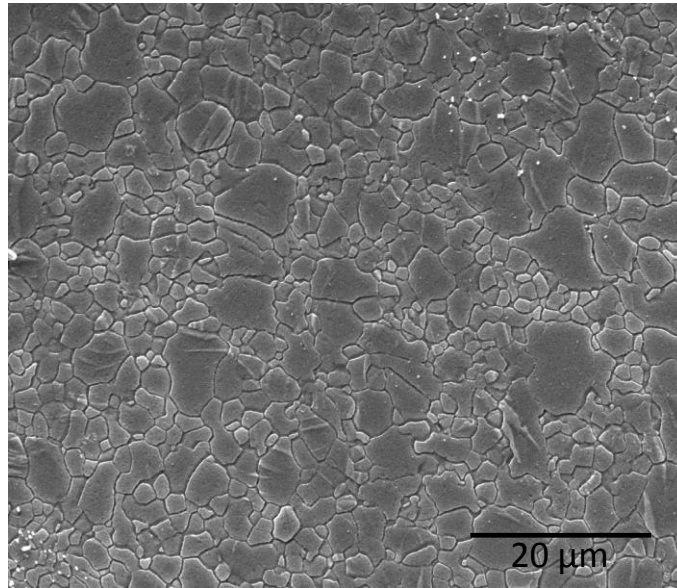
Figure 18. Secondary electron micrograph of AZ31 plate processed 4A.

While we expected repeatability for A and C routes, Routes B and B_c are another matter. Furukawa et al [50] and Segal [59,60] illustrated the differing shear paths when repeatedly rotating 90° about the plate normal rather than the bar axis. Segal postulated that despite a set of four passes causing shearing on two planes, plate B_c would be less effective at grain refinement than bar processing [60]. While this might be the case, the differences in strain path are much more significant to ECAE processing of anisotropic materials like magnesium. Again working at 200°C, a plate of AZ31 was processed through $4B_c$. Figure 19 illustrates the microstructure, compressive response, and associated basal texture of the plate. As in the bar case, the average grain size is slightly more refined by route B_c than route A at this temperature. The mechanical response is substantially similar to the $4B_c$ bar compression results shown in Figure 8 but the texture

is somewhat different. Like the bar case, the texture is still relatively weak/spread, but there is a high concentration of basal poles towards the plate normal. In both cases there is a tendency to rotate the basal poles from the previous shear plane to the new one, and the total rotation required is the same. The orientation from which the bulk of those grains are rotating in a given pass is what results in this variant of the spread texture.
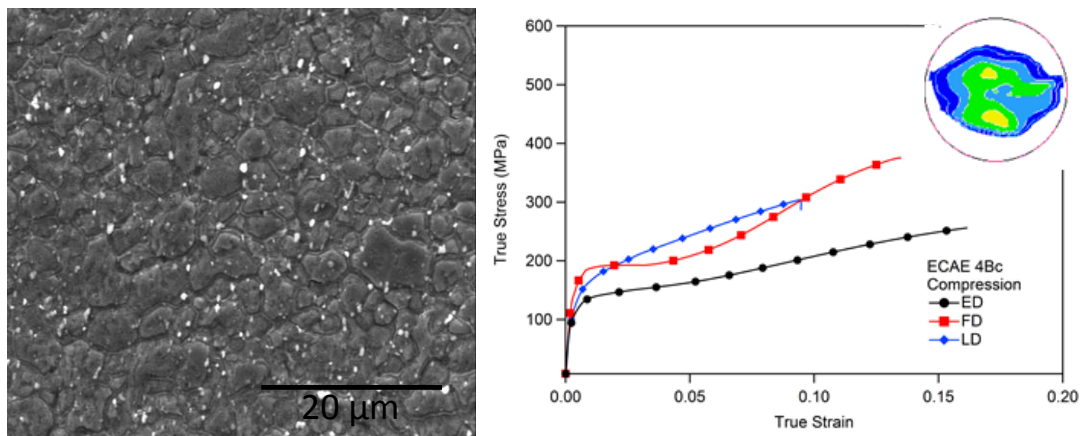
Figure 19. Microstructure, basal pole figure, and compression stress-strain response of AZ31B plate processed via 4Bc at 200°C . Unlike other cases in this chapter, the pole figure is taken from the plate normal/LD with ED to the right and FD below in order to better capture the texture character.

Having established the capacity to accomplish simple ECAE operations on AZ31 plate, we moved on to hybrid route processing. While we were prohibited from accessing the lowest temperatures used in 5H and 7H, we were able to produce C-type and A-type textures in plate material. Figure 20 depicts the mechanical response and texture for an A-type material processed through four DRX-promoting passes followed

by two basal + non-basal slip promoting passes. Comparing the mechanical strength of this material to that of the 4A plate, yield strengths have increased by ~50% in the three orthogonal directions. The story is similar for the C-type hybrid plate properties in Figure 21, although here only the FD compression yield strength is significantly higher. The other two directions, which we expect to yield almost exclusively by basal slip, are less affected by the microstructural refinement. More details on this matter will be discussed in Chapter III.
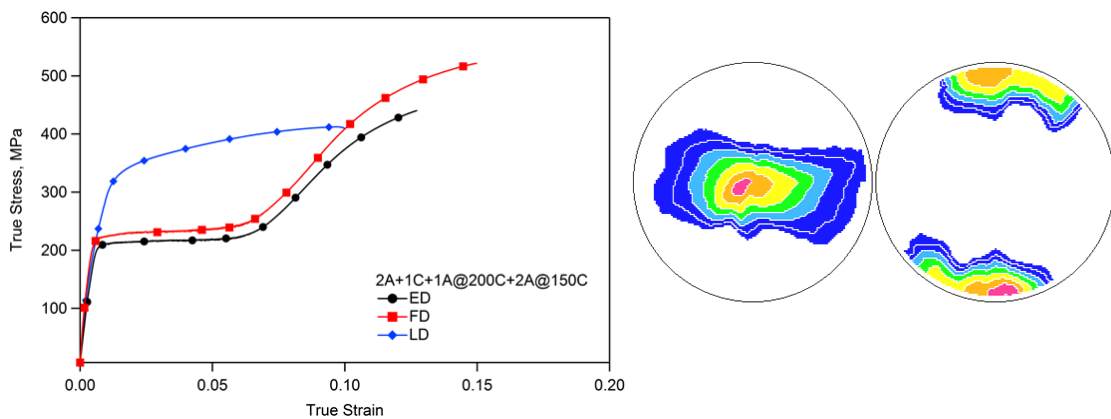
Figure 20. Compression response with prismatic and basal pole figures of AZ31B plate processed via hybrid route 2A+1C+1A at 200ºC followed by 2A at 150ºC. This is an example of the A-type texture.
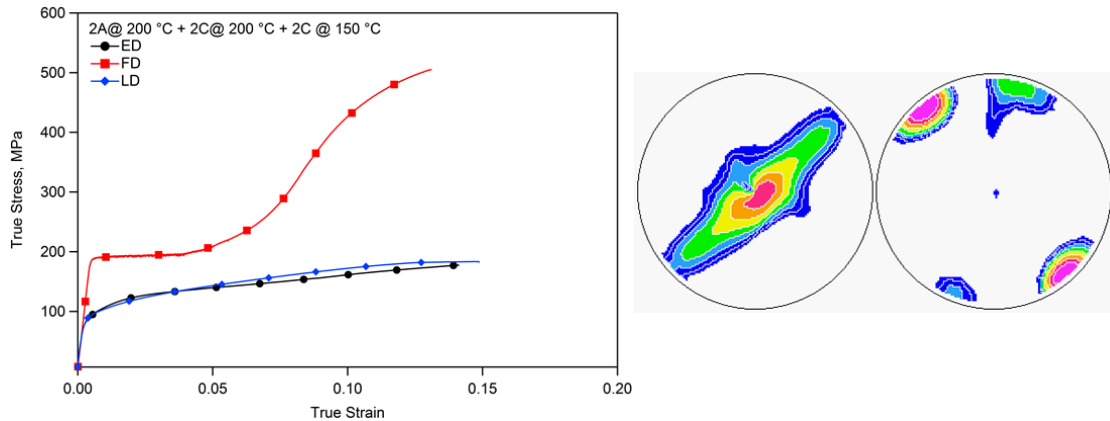
Figure 21. Compression response with prismatic and basal pole figures of AZ31B plate processed via hybrid route 2A+2C at 200°C followed by 2C at 150°C. This is an example of the C-type texture.

Expected and Unexpected Problems Encountered with ECAE Processing

Tool temperature uniformity

Given the temperature dependence of CRSS ratios depicted in Table 2, it is clear that ECAE processing of AZ31 requires tight temperature control. Indeed, when we began processing bars, the unheated bottom wall of the exit channel was identified as a significant contributor to non-uniform deformation. This issue was alleviated with the addition of another heater and controller. The plate case, however, did not provide a simple solution. The top surface generally, and the nose of the plate particularly, would frequently suffer from cracking during the first pass. Occaisionally cracks were also observed in the bottom surface or deep cracks at the tail end of the billet after additional passes. Most of the surface cracks were shallow, but in one case the nose crack was severe enough to shear the ~45° unprocessed section off from the rest of the plate. A

44

representative plate is pictured in Figure 22. This phenomenon occurred during the first

pass but the cracks persisted throughout additional extrusions. Heating the die and plate

to 230°C, rather than 200°C, for the initial pass solved the problem. While higher

temperatures would certainly increase the availability of nonbasal slip, the need for this

additional temperature was surprising given that we did not experience the issue at

200°C in the bar tool. A survey of the plate tool temperature uniformity revealed a tight

(<5°C variance) temperature control around the surface of the inlet channel. The bottom

channel had a problem with cold spots (up to 10°C lower than set temperature), but

increasing the temperature by up to 20°C had no affect on first pass cracking. While

these large cracks at the nose and edges reduced the product yield, the surface cracking

had no apparent impact on the bulk properties.

Figure 22. Photograph of AZ31B plate with multiple top surface cracks after ECAE processing. Punch face is on the left and extrusion direction is to the right.

Chemical Uniformity

The first extrusions we performed utilized donated material from Magnesium Elektron. Our typical approach with difficult-to-work FCC/BCC metals is to process just below the recrystallization temperature in an attempt to maximize ductility without triggering grain growth. We knew that others had seen recrystallization at $200^{o}C$ but were not able to process at lower temperatures in the AZ31 and ZK60 alloys of interest. This being a simple set of extrusions for us to begin our investigation with, we used $200^{o}C$ and $150^{o}C$ as the processing temperatures, and 4E as the strain path. The $150^{o}C$ material did not fare well, with cracking and shear localization probems immediately apparent in the load curves. At $200^{o}C$, processing was possible but did not accomplish much in terms of grain refinement (our initial goal). A close examination of the materials was conducted using wavelength dispersion spectroscopy hinted at part of our problem. The chemical segregation seen in Figure 23 was far worse than the batches of AZ31 that we later examined. It appears to have been so severe in these cases that the expected dynamic-recrystallization induced grain refinement was inhibited. In the AZ31B, the purple is Al and Zn enrichment near the grain boundaries. Examining the phase diagram, this is a consequence of slow-cooling during casting. The ideally 3% and 1% levels of Al and Zn in this alloy were far lower in the dark areas, dropping to unmeasurable levels in grain interiors. Since Al and Zn are both solid-solution strengthening additions, this is likely to be a significant contributor to non-uniform deformation. The yellow and green particles are due to an excess of Mn addition, which is used to precipitate out iron from the melt. In the ZK60A the green Zn is again at the cast grain boundaries, indicating

46

slow cooling and non-uniform matrix strength. The small number of Zn-Zr seem unlikely to have had an impact. The images, taken from the flow plane, clearly reveal that even at 200°C the chemical segregation caused shear localization. Note the near-vertical lines of interrupted flow in the processed AZ31B, markers of shear banding. This shear banding was even more pronounced and widespread in the 150°C case, and almost no deformation occurred between these bands. The ZK60A had voids in the starting material which, while difficult to see after processing, were not completely eliminated. However, there were few shear bands (unlike the 150°C case). Despite the capabilities of this severe plastic deformation process, the quality of starting material can severely restrict formability. Sometimes free material is worth exactly what it costs.
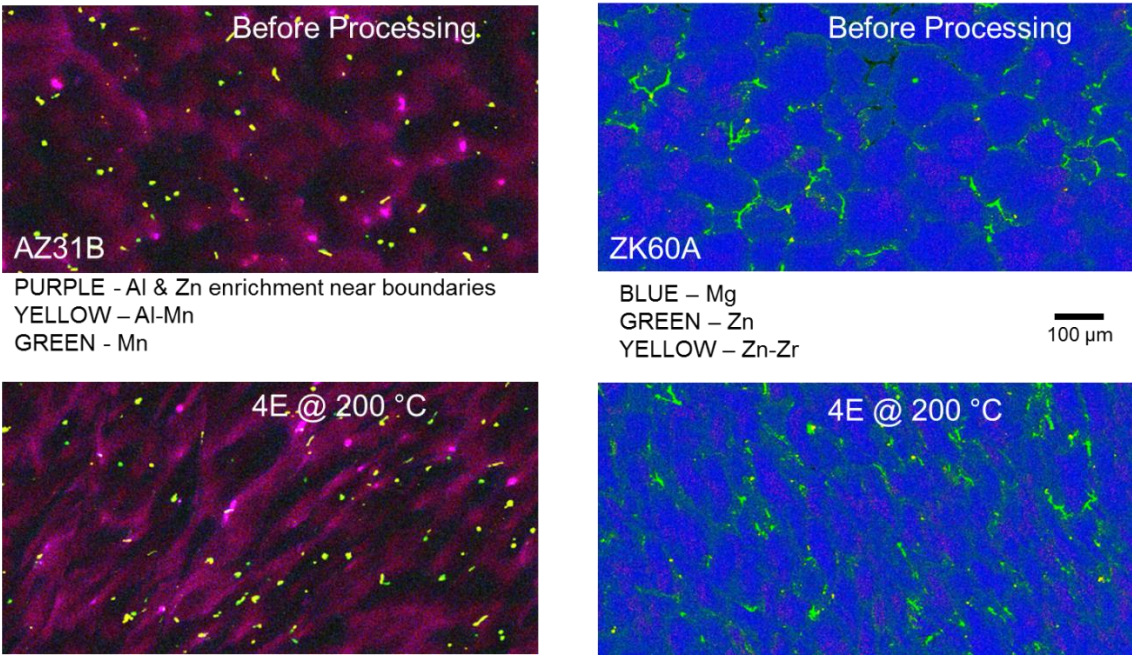
Figure 23. WDS chemical maps of magnesium alloys AZ31B and ZK60A in as-received and processed conditions.

In the case of ZK60, even material that deformed relatively well exhibited a large degree of chemical non-uniformity. Figure 24 contains optical micrographs of extruded ZK60A from Timminco in the as-received condition as well as after a homogenization attempt. This homogenization consisted of a 15 hour anneal at 500°C followed by two passes Route A through a 500°C isothermal ECAE die. The appearance of a second phase is largely eliminated but small "stringers" of second phase material appear as near-horizontal groups. Figure 25 contains back-scatter electron images of these two conditions, highlighting the remaining, if reduced, enriched phase. WDS analysis indicated that the brightest regions in the as-received condition were 2.7-3.1%Zn, 0-0.7% Zr while the darkest regions were ~1.7% Zn, 0.7% Zr (atomic %). After the homogenization attempt the darker areas pickup up almost 0.1% Zn and the bright areas were generally ~2.2% Zn with an overall smaller area fraction of enriched material. We were never able to fully homogenize the alloy but further efforts yielded substantial grain refinement and mechanical property improvement after ECAE processing.
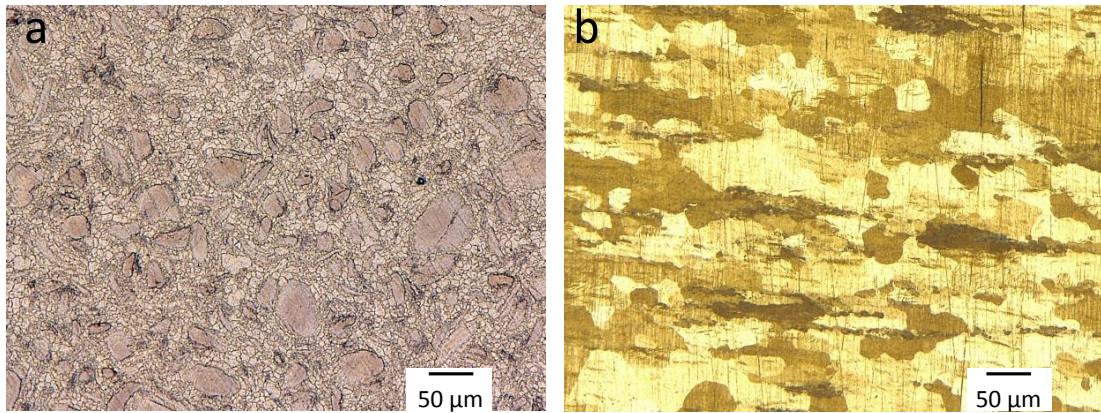
Figure 24. Optical Micrographs of ZK60 in (a) As-received condition, transverse plane, and (b) Homogenization Attempt condition, flow plane.
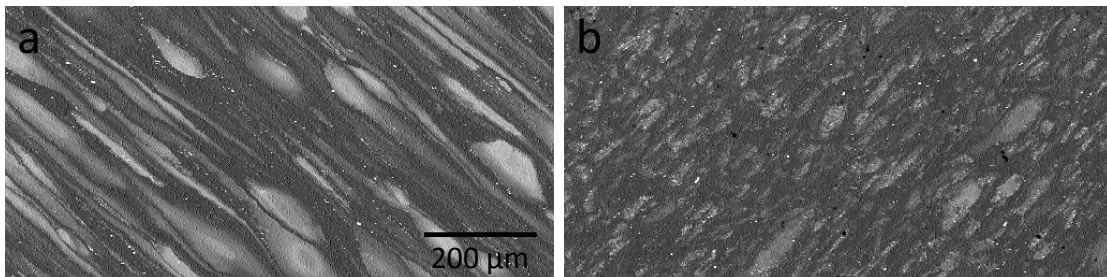
Figure 25. Back-scattered electron images of ZK60A in (a) As-received condition, longitudinal plane, and (b) Homogenization attempt, flow plane.

The most severe case of chemical segregation that we observed during the Mg development effort was in rolled WE43 plate. In Figure 26 the rolled nature of the product is evident when observed from the transverse plane. The sheets of Zr remained evident even after an 8hr heat treatment at 525°C. We attempted to extrude the material in the as-received condition up to 300°C, including utilizing canning and backpressure,

49

resulting in cracking and destruction of the bars cut from the plate. We then attempted to anneal the material at $>0.9T_m$ but found that even a 12h 550°C anneal followed by extrusions at 525°C and 550°C in our isothermal tooling did not address the issue. This was surprising to the author given that we were processing on the nose of the "melting range" quoted by the manufacturer, 540-640°C [61] and at what might be described as a glacial pace. In fact, we were slower, as in one case the rate was 8h to complete an extrusion on a 125mm bar while the relatively speedy Jakobshavn glacier in Greenland was recently measured as moving at 20m/day [62]. It is therefore not shocking that the factory has a great deal of difficulty with rolling this alloy.
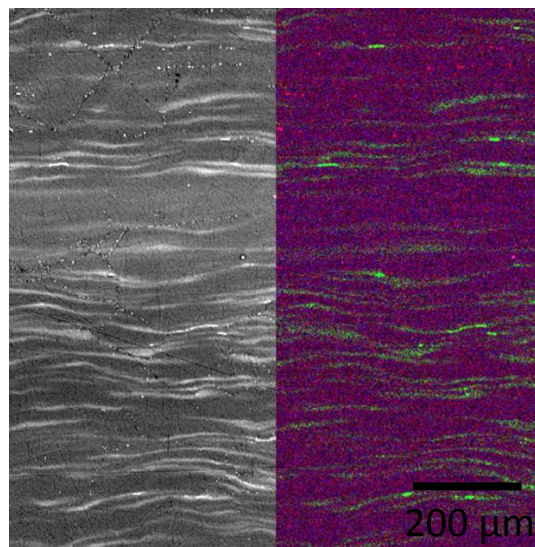
Figure 26. Secondary electron micrograph and WDS chemical map of WE43 plate. Rolling direction is horizontal and plate thickness is vertical. Sheets of green Zr enrichment are visible with Y particles decorating the grain boundaries and Nd dispersed relatively uniformly.

Conclusions

We demonstrated methods to refine grain size in Mg alloy down to sub-micron levels using severe plastic deformation. Using different routes and combinations of routes allows for the selection of deformation mechanisms and the generation of different textures. This effort produced AZ31 with variations in yield strength anisotropy and a significant improvement in strength. The work allowed us to further study the impact of grain size on magnesium deformation, the topic of Chapter III. We achieved yield strengths of 250+MPa in a ZK60 material with anisotropy approaching that of steel sheet product and yield strength up to the 350MPa goal set by our sponsor, U.S. Army Research Lab. The work in this chapter provides a basis for production of wrought Mg alloy with grain sizes and textures unachievable with conventional methods.

CHAPTER III

THE INFLUENCE OF GRAIN SIZE ON DEFORMATION MECHANISMS

Introduction

Magnesium is a promising structural material for lightweight applications as its density is one fourth that of steel. Commercially available Mg alloys have specific strengths (per weight) above that of mild steel but there is a gap between current performance and what is needed to replace high-strength steel, aluminum, or titanium alloys in many applications [63]. While much of the current development work in this area focuses on adding rare earth alloying elements, significant strength gains have been achieved in wrought alloys through grain refinement [55,64-73].

The mechanical behavior of magnesium and Mg alloys has long been known to be highly dependent on crystallographic orientation [74-76]. The limited number of slip systems and high critical resolved shear stress ratios between the possible deformation mechanisms result in severe mechanical anisotropy in the wrought materials. Additionally, there are multiple geometrically necessary twinning mechanisms which are directional in nature and these lead to tension/compression asymmetry [77-79]. The present study sheds light on the grain size dependence of different deformation mechanisms in a 3%Al-1%Zn Mg alloy, nominally, AZ31B by testing samples with similar textures but with an order of magnitude difference in grain sizes.

In this work we have utilized equal channel angular processing (ECAP) to refine grain size. Although only one texture is shown in this work, several studies have examined the various textures and resulting mechanical properties produced by changing the strain

path (route) during ECAP [57,70,80-84]. At elevated temperatures ($\geq$200 ^{o}C), ECAP has been utilized to improve the mechanical isotropy [85] and formability [86] of Mg alloys. Unfortunately, the limited number of slip systems available in Mg alloys make it difficult to process these materials below around 200 ^{o}C, at which most of the ECAP work in the current literature was performed. At lower temperatures issues such as strain localization, also known as shear banding, have been widely reported [34,87,88]. Fortunately, tooling developments such as back-pressure application, made it possible to suppress this phenomenon and further expand the processing envelope [34]. Additionally, straying from conventional ECAP schedules and utilizing temperature step-down methods have provided the means to process Mg at lower temperatures [37,57,70,89,90]. For pure Mg, room temperature processing is possible using the temperature step-down approach [42]. These advancements have resulted in stronger materials, such as AZ31B with a 385 MPa tensile yield strength [57].

It has long been known that Mg and its alloys do not follow a single Hall-Petch slope as cubic materials typically do because of their intrinsic mechanical anisotropy [91]. Barnett et al. changed the processing parameters for conventional extrusion to generate AZ31 samples with average grain sizes ranging from 3 to 23 μm [92]. In addition, they controlled the activation of slip or twinning during mechanical tests by varying the testing temperature. At 150 ^{o}C they observed that the 3 and 4 μm average grain size material did not twin significantly compared to the larger grain size materials. Further, they demonstrated that the H-P slope changed drastically when slip overtook twinning as the primary deformation mechanism. It appears that all metals are more

sensitive to grain size when twinning occurs as compared to dislocation slip [93].

Barnett et al. [92] proposed that the initial plastic deformation mechanism is determined

not only by the Schmid factor, but also grain size, temperature, and strain rate. Also,

they demonstrated that at elevated temperatures twinning is suppressed below a certain

grain size (depending on deformation conditions). The results implied that this

suppression of twin formation could be accomplished at room temperature given a

sufficiently small average grain size. Other work also conducted at elevated temperature

showed that when twinning is suppressed, the tension/compression yield strength

asymmetry is eliminated [77]. In a study of rolled AZ31B sheet, Jain et al. pointed out

that it is difficult to measure the grain size dependence of different slip mechanisms

from the H-P slope alone, and used neutron diffraction to probe deformation activity

during uniaxial tension or compression [73]. Although they did not observe a transition

in the yield mechanism, they did note that twin volume fraction in deformed samples

increases with increasing grain size. The present study will observe both the initial

deformation mechanisms and twin volume growth at room temperature, under

compression in three orthogonal directions using significantly finer grain size than

previously studied, in order to establish room temperature twin suppression

Materials and Methods

Materials and Processing

The starting material used in this chapter was the 2C and 5H material, the

processing for which was described in Chapter II. The samples were made via ECAP of

commercially available AZ31B hot-rolled plate with an initial average grain size of 25

54

µm and a typical grain size range of 10-70 µm, as well as the usual plate texture with basal poles aligned with the plate normal. Figure 27 shows a schematic of the sample orientation and initial texture relative to the die coordinates during ECAP. The thermo-mechanical process schedule is presented in Table 3. The processing schedule and temperature step down method for the fine grain material were selected to refine the grain sizes below 1 µm while resulting in the final texture of the coarse grain material. Since the rotations are a combination of typical ECAP routes A and C, the authors refer to this and other such combinations as "hybrid" routes [57,70,94]. The rotations described in Table 3 are about the bar's long axis prior to re-insertion and the bars were held 20 minutes in the inlet channel to reach the temperature of the die prior to actual processing. The die used has a sharp 90° intersection angle (φ in Fig. 1) and is equipped with a backpressure system that maintained ~35MPa on the material as it passed through the shear zone.
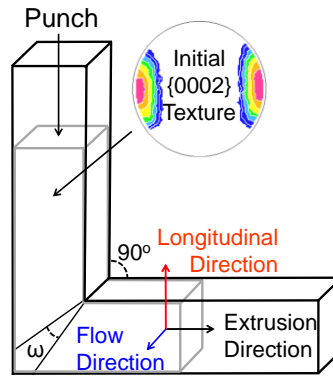
Figure 27. Schematic of ECAP process illustrating the workpiece passing through a sharp 90° angle with the shear zone defined by the arc ω. The {0002} texture of the starting plate material is indicated in the inlet channel to illustrate the initial crystal orientation with respect to the bar axis. The directions illustrated about the exit channel correspond with the samples tested for this study and will be referred to with abbreviations LD, FD, and ED.

Table 3. ECAP of coarse-grained and fine-grained AZ31B samples detailing the ECAP temperature for each pass. The rotation angle is about the long axis of the workpiece, prior to reinsertion for the given pass.

Fine-Grained	Pass 1	Pass 2	Pass 3	Pass 4	Pass 5
Rotation	0°	0°	180°	0°	180°
Temperature	200°C	200°C	150°C	150°C	125°C
Coarse-Grained	**Pass 1**	**Pass 2**			
Rotation	0°	180°			
Temperature	200°C	200°C			

Characterization Methods

Optical and secondary electron micrographs (SEM) were prepared using a picral

etch after mechanical polishing [43]. Transmission electron micrographs (TEM) were

prepared from 3 mm discs, ground to 100 µm then thinned using a twin-jet polisher with

56

a 5% $HClO_4$/methanol solution. Texture measurements through X-ray diffraction were performed using a Bruker AXS D8 Discover diffractometer with a Cu-K$_\alpha$ source operating at 40 kV and 40 mA. Compression samples were 10 mm in diameter and 24 mm in length. The directions and labeling of these samples are illustrated in Figure 25. Three directions were examined in compression: the extrusion direction (ED), flow direction (FD), and longitudinal direction (LD).

Neutron diffraction was carried out at the Lujan Neutron Scattering Center (LANSCE) at the Los Alamos National Laboratory on the mechanical test samples described above. The High-Pressure Preferred Orientation diffractometer (HIPPO) was used to generate orientation distributions before and after in-situ deformation. In-situ deformation was performed in the Spectrometer for Materials Research at Temperature and Stress (SMARTS). The SMARTS system generates diffraction data using detector banks aligned to capture diffraction patterns with axial and transverse diffraction vectors as illustrated in other works using the instrument for Mg alloy measurements [95,96]. Samples were deformed under displacement control, moving to a given crosshead position then holding for a period of 20-45 minutes for diffraction data collection, depending on the flux of the neutron beam, before moving to the next strain value. Since stress was allowed to vary over time at a given strain value, a time-averaging technique was used to represent the stress recorded by the SMARTS load frame. Inverse pole figures were generated from the SMARTS diffraction data using the SmartsWare software suite.

Results

Texture and Microstructure

The starting material from which the two groups of samples were created has a typical rolling texture, shown in Figure 28a with the texture of the two ECAP processed materials also shown in Figure 28b and Figure 28c. Examining only the basal pole figures, it is apparent that the coarse-grained and fine-grained textures are quite similar, the main difference being a slightly weaker character in the fine-grained samples. Despite the differences in the processing temperatures, the textures are very similar because the last two passes of the fine-grained material route follow the same ECAP route as used to generate the coarse-grained material. During ECAP multiple deformation mechanisms are active and two primary orientations are generated. From visco-plastic self consistent crystal plasticity modeling predictions [6], we expect the deformation to be dominated by basal slip. This dominance produces a larger fraction of grains oriented with their basal planes aligned with the ECAP shear plane.
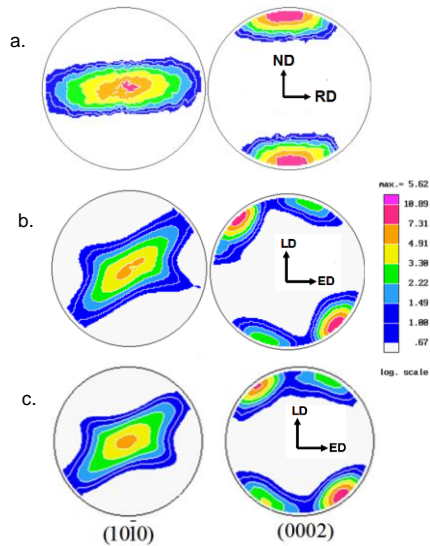
Figure 28. Prismatic and basal pole figures of (a) plate material prior to processing, (b) coarse-grained (5.5 μm), and (c) fine-grained (0.78 μm) after ECAP following the processing schedules listed in Table 1.

Figure 29a shows a micrograph of the coarse-grained material. Occasional large grains remain as islands among newly-formed 1-5 μm grains resulting in an overall average grain size of 5.5 μm. An additional two passes at 200 ^{o}C would produce an essentially uniform 1-5 μm microstructure, as shown in our previous work [22]. The lower temperature and additional straining in the processing of the fine-grained bar further refines the microstructure as seen in Figure 29b. While grain size statistics are shown, some of the etched surface is difficult to resolve so the 0.78 μm average grain size may be larger than the actual grain size average. Transmission electron microscopy (TEM) allows for a more detailed examination of the fine-grained microstructure. Although obtaining statistically significant grain size data from TEM micrographs is difficult, the features shown in Figure 29c are primarily true grains, as indicated by their

variation in contrast. These grains appear to be closer to 0.5 μm under TEM. Although a

few twins were found, they were rare in the microstructure of either material.
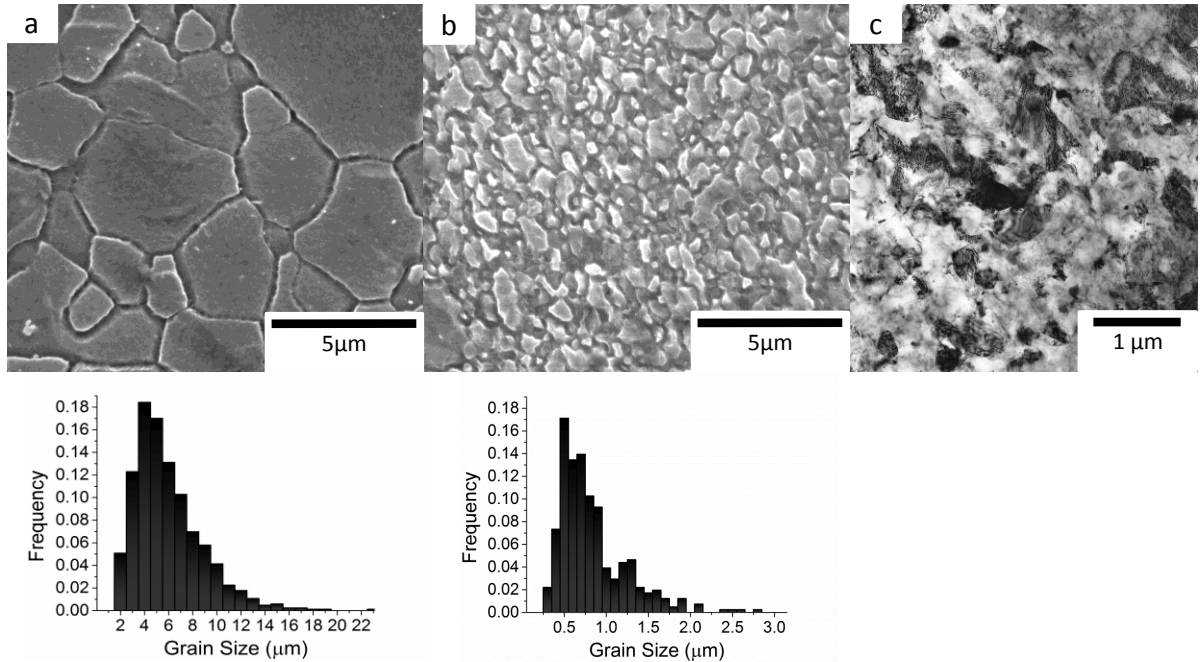
Figure 29. Secondary electron micrographs with corresponding grain size histograms of (a) coarse-grained and (b) fine-grained samples and (c) transmission electron micrograph of the fine-grained material.

In-Situ Mechanical Response

While quasistatic mechanical testing of the coarse-grained and fine-grained

materials has been presented elsewhere [43,70], the discussion here focuses on the in-

situ mechanical response. Therefore, the stress vs. strain response during neutron

diffraction is presented in Figure 28. In the flow direction (FD) samples in Figure 28a,

the coarse-grained sample initially undergoes no hardening after the yield point, but later

demonstrates a strong hardening response. The hardening-free plateau is extended

further during deformation of the fine-grained sample and, although some hardening is

evident, does not reach significantly higher stress levels than the yield stress. In the

extrusion direction (ED) samples, a gradual hardening is observed in both the coarse-

grained and fine-grained cases and the longitudinal direction (LD) fine-grained sample

appears similar. There are notable differences in these results as compared to the

previously conducted conventional mechanical test results. Most significant of these are

the load drops corresponding with the strain values at which the neutron data were

collected. These drops are more severe when the beam flux was low, requiring more

time to collect sufficient data, and grew with higher stress levels. There are also

differences related to the material performance. Most notably in the FD samples of

Figure 30, the fine-grained sample fractured at a strain of 11% rather than the ex-situ

average of 16%. Other samples may have also fractured earlier than those for the ex-situ

testing, but they were not strained to failure.
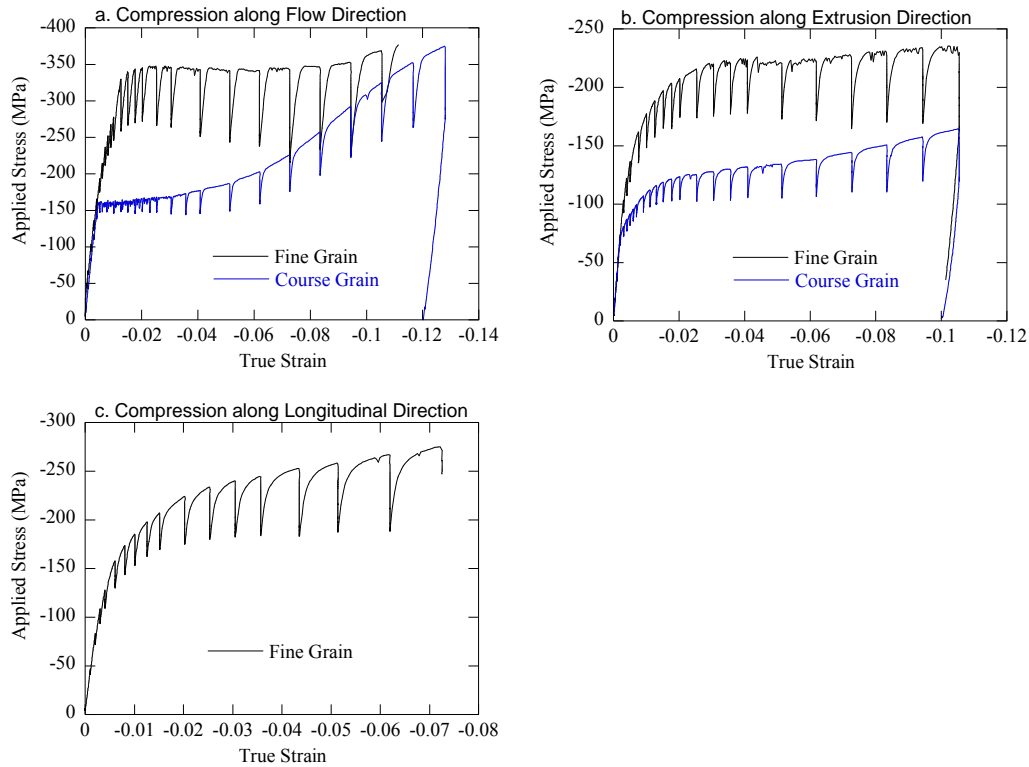
Figure 30. In-situ compression testing of AZ31B Mg Alloy during neutron diffraction measturements along the three orthogonal directions (a) FD, (b) ED, and (c) LD.

Texture Evolution

In order to ensure that the in-situ diffraction data were representative of overall trends, pole figures were generated before and after testing for each sample. As shown in Figure 31, most of the basal poles in the extrusion direction samples are at 40-60° from the compression direction. The $\{0002\}$ poles rotate slightly towards the compression axis after compression. In constrast, the basal poles of most grains are perpendicular to the compression axis in the flow direction samples. In the coarse-grained case, these are completely reoriented after compression such that the basal poles are alligned with the

62

compression axis. Although most grains in the fine-grained sample behave similarly, a small population of grains are rotated from perpendicular towards the compression axis rather than reorienting along the compression axis. Finally, the weak "bridge" between the two basal poles groups is strengthened in the longitudinal direction sample while the peaks rotate towards the compression axis.
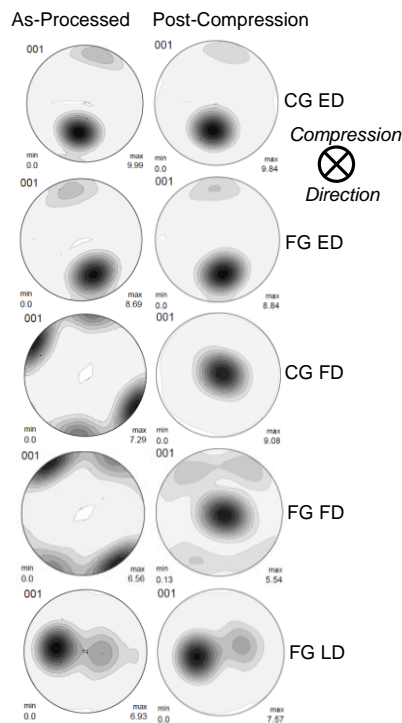
Figure 31. Basal pole figures generated by HIPPO before and after in-situ compression testing. The ED and LD samples undergo minor reorientation during compression while the FD samples experience an essentially perpendicular shift towards the compression axis.

The inverse pole figures in Figure 32 are representative of a larger data set collected during in-situ testing of the coarse-grained samples. They indicate pole density

63

along the compression direction and are also representative of trends in the fine-grained

sample. Figure 32a shows the response of the FD sample from the coarse-grained

material. As the strain increases from top to bottom, the initially $\{10\bar{1}0\}$ oriented grains

flip to a basal orientation without significantly populating the intermediate orientations.

The inverse pole figure of the ED sample is represented by Figure 32b, and clearly

shows a continuous rather than discrete orientation evolution. The two series of inverse

pole figures correlate well with the start and end full basal pole figures shown in Figure

29.
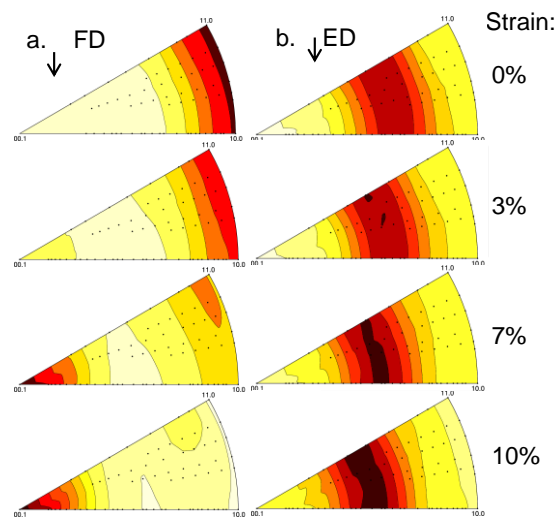
Figure 32. Examples of inverse pole figure progression (looking down the compression axis) during compression of (a) coarse-grained FD sample in which there is a nearly complete reorientation without intermediate orientations and (b) coarse-grained ED sample which exhibits a gradual change in texture during compression.

64

Lattice Strains

Lattice strain measured by neutron diffraction vs. true strain is shown in Figure 33a-c for the in-situ compression samples along the three orthogonal directions. These lattice strains reflect only the elastic deformation (change in lattice parameter) of the crystallites. Thus, large deviations between the measured lattice strains and the macroscopic elastic strain indicate inelastic deformation. A solid line representing a one-to-one correlation between compression and lattice strains has been inserted into Figure 33a-c to highlight the initiation of yield. The lattice strain in the compression direction for several crystal orientations are plotted versus the overall strain applied to the compression sample. It is important to emphasize that the data are taken from grain populations with specified planes oriented normal to the compression axis, as opposed to a lattice strain measurement for all such planes in the samples.
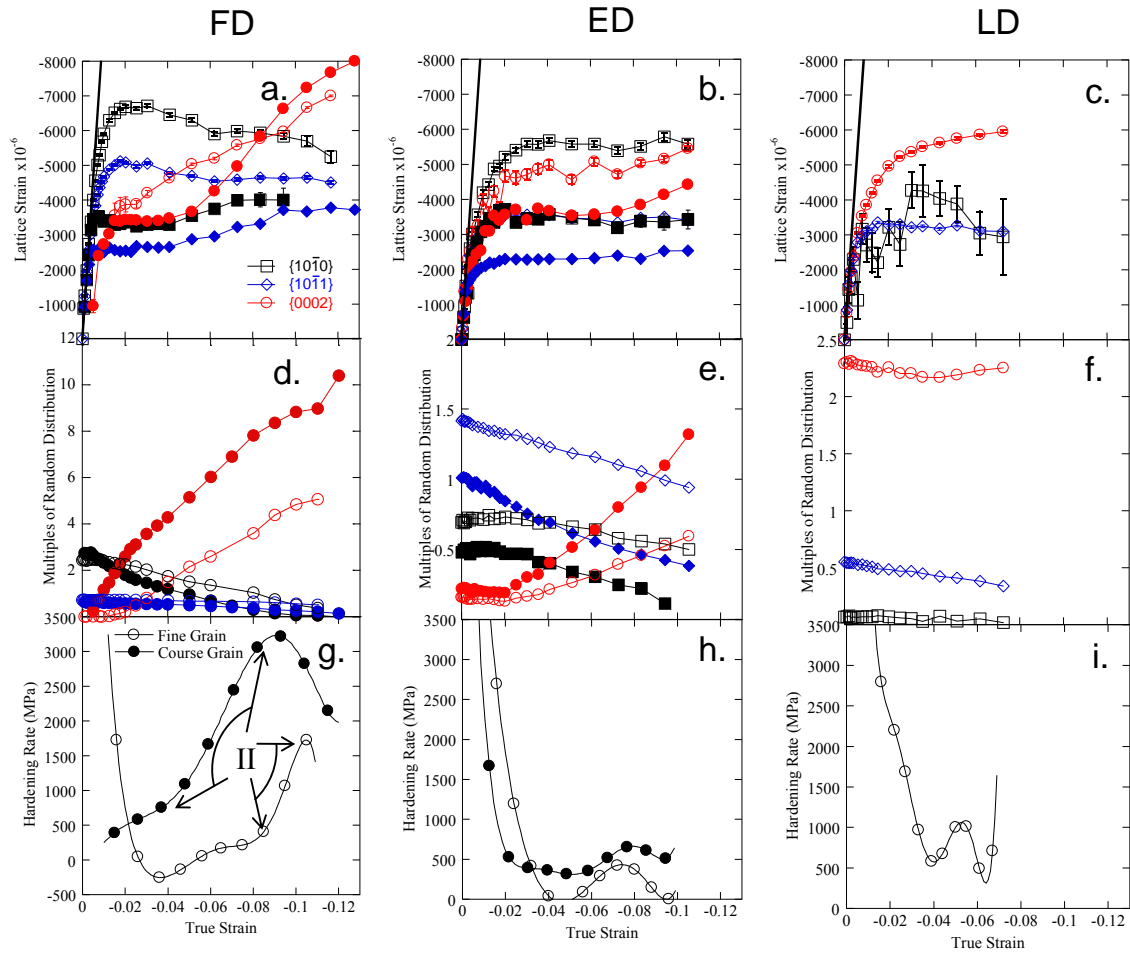
Figure 33. Lattice Strain vs. True Strain curves for in-situ compression of the (a) FD, (b) ED, and (c) LD samples with the solid black lines representing the one-to-one correlation (elastic behavior). In all diagrams, open and filled symbols represent fine-grained and coarse-grained materials, respectively. Diffraction intensity vs. true strain plot for in-situ compression of the (d) FD, (e) ED, and (f) LD samples highlighting the drastic reorientation in the FD samples compared to the others. Hardening rate vs. true strain plot for in-situ compression of the (g) FD, (h) ED, and (i) LD samples represents the first derivative of the corresponding true stress vs. true strain traces in Figure 30.

Figure 33a shows the lattice response of the FD samples. The strains in grains

oriented with $\{10\bar{1}0\}$ and $\{10\bar{1}1\}$ along the compression axis for fine-grained material

(open symbols) depart from the initial linear response at a much higher strain than in their coarse-grained counterparts (full symbols), much like the macro stress vs. strain traces. Data for the basal plane compression case are initially absent since there were essentially no grains oriented with their $\{0002\}$ poles in the compression direction.

Although strains in both $\{0002\}$ populations eventually climb, there are significant differences in their initial measurement. For the coarse-grained material the basal population appears at the same macro strain level at which the other planes deviate from the elastic line. This $\{0002\}$ population initially has a relatively low lattice strain level but quickly climbs to a plateau at 3500 $\mu\varepsilon$ where it stays through 4% true strain before climbing further. The fine-grained $\{0002\}$ lattice strain, on the other hand does not appear until a true strain of 1.5%, well after the other planes have indicated a departure from elasticity. While the initial fine-grained lattice strain correlates with the coarse-grained value at that true strain level, the fine-grained $\{0002\}$ planes immediately begin to compress further rather than exhibiting a plateau similar to the coarse-grained sample. A more subtle difference between the coarse-grained and fine-grained lattice strains is the way in which the strains in $\{10\bar{1}0\}$ and $\{10\bar{1}1\}$ oriented grains deviate. While the coarse-grained traces immediately plateau, strains in the fine-grained material continue to increase until the 1.5% true strain level at which the $\{0002\}$ population appears. Further, the coarse-grained $\{10\bar{1}0\}$ and $\{10\bar{1}1\}$ grains eventually undergo a modest increase in lattice strain while those in the fine-grained actually decrease. Lattice strains

67

in $\{0002\}$ oriented grains reach higher levels than the other populations for both grain sizes.

Although the ED samples have only a small fraction of $\{0002\}$ poles aligned with the compression direction, as indicated by the pole figures in Figure 31, there are enough grains so oriented initially such that the $\{0002\}$ peak is observable. Figure 33b shows that the traces for all three lattice planes in both samples deviate from the elastic line in the same way as the fine-grained FD $\{10\bar{1}0\}$ and $\{10\bar{1}1\}$ strains, continuing to higher strain levels until they level off. While the fine-grained samples go to higher lattice strains than their coarse-grained counterparts, the $\{10\bar{1}0\}$ and $\{10\bar{1}1\}$ strains remain essentially flat and the $\{0002\}$ strains undergo only a modest increase during compression. The fine-grained LD sample in Figure 33c exhibits similar behavior to the ED samples, although the $\{0002\}$ strain never reaches a steady level. Also, the population of $\{10\bar{1}0\}$ oriented samples is too low for confident identification of any trends in that lattice strain. Finally, all of the $\{0002\}$ lattice strains qualitatively correspond with their stress vs. strain traces in Figure 30.

The pole density data presented in Figure 33d-f are essentially another way of looking at some points on the progression of inverse pole figures in Figure 32. However, this presentation allows for a more direct comparison with the lattice strain and macroscopic hardening rate. In all cases, the $\{10\bar{1}0\}$ and $\{10\bar{1}1\}$ intensities are

declining throughout the compression although this decrease is minimal for the LD

samples since there is a low signal along the compression axis to begin with. Therefore,

the $\{0002\}$ intensities will be the focus of these three plots.

The FD samples initially have no significant grain population with $\{0002\}$ poles

oriented along the compression axis. However, the population immediately begins to

grow in the coarse-grained sample upon straining, increasing to an intensity of 10.3

multiples of random distribution (MRD) at the end of the test. On the other hand, the

$\{0002\}$ pole density in the fine-grained sample does not increase above 0.5 MRD until

2% strain, and only reaches 5.1 MRD at the last data collection point before sample

failure. The $\{10\bar{1}0\}$ and $\{10\bar{1}1\}$ traces drop nearly or completely to zero in both FD

samples.

In the ED samples, the $\{0002\}$ intensities are initially near zero and only begin to

increase after 2% true strain in both cases. While the coarse-grained sample begins to

align $\{0002\}$ poles with the compression axis more quickly than the fine-grained sample,

both end with intensities below 2 MRD, which is consistent with Figure 31. The fine-

grained LD sample had a small population of basal poles aligned with the compression

axis to begin with which remained almost unchanged during testing.

The hardening behavior plotted in Figure 33g-i were generated by fitting a

polynomial curve to the macro stress-strain data in Figure 30 having removed the load

drops during neutron collection. The first derivative of this polynomial is shown in the

figure. This highlights some trends that would otherwise be difficult to observe in Figure

30. In both the ED samples of Figure 33b, the hardening rate is quite low after the initial

departure from elastic behavior, remaining low until the end of the test. The LD sample

in Figure 33i has a slightly higher hardening rate. However, the FD samples show a

much different trend. The coarse-grained hardening curve does not have the extended

initial drop region that the other four curves exhibit because the sharp transition from

elastic to a plastic plateau in the stress vs. strain trace of Figure 30a prevents a good

polynomial fit at this point. The curve presented here is nevertheless representative of

the mechanical behavior during plastic deformation and is only missing a near-vertical

drop at the beginning of the coarse-grained curve. While the coarse-grained hardening

remains in the range of the ED and LD samples until about 5% true strain, the hardening

rate does not climb in the fine-grained sample until 9-10%, shortly before fracture.

Further, the hardening rate in the fine-grained sample is nearly zero. Finally, the slopes

of the coarse-grained and fine-grained hardening rates are nearly identical in the sections

marked as II in Fig. 7g.

A more traditional method of plotting the lattice strain data is presented in Figure

34 in order to allow for comparison with other studies and clarify trends in the

diffraction data. Lines representing the elastic modulus (approximated as 47GPa) have

been added in order to clarify these trends. Lattice strains observed during compression

of the coarse-grained and fine-grained FD samples are shown in Figure 34a and b,

respectively. In the coarse-grained samples the traces for all but the $\{0002\}$ go

essentially vertical after deviating from the elastic line. The $\{10\bar{1}1\}$ is first to deviate

near 100 MPa and the $\{10\overline{1}0\}$ does not deviate until 150 MPa, the stress level at which the basal poles appear. The grains associated with these incipient basal poles are at a low lattice strain, but there is a plateau until the lattice strain reaches the elastic modulus. The $\{0002\}$ lattice strain levels then increase, while the others do not increase with stress. In the fine-grained sample the $\{10\overline{1}1\}$ also deviates at a much lower stress than the other systems. However, unlike the coarse-grained material the $\{10\overline{1}0\}$ only departs this line at a high stress level. Sample volume with $\{0002\}$ orientation appears at ~285MPa stress level and increases in lattice strain as the stress levels drop corresponding to the time-averaged load during neutron data collection. For the ED samples in Figure 34c and d the lattice strain values spread from the elastic modulus to a similar degree. However, the spread of the coarse-grained lattice strains is larger and more immediate than for the fine-grained sample. The LD sample appears similar to the ED samples with the $\{0002\}$ taking the most strain (there was not enough $\{10\overline{1}0\}$ signal in the LD sample to measure lattice strain in that direction). Finally, a trend across all the samples is that the $\{0002\}$ generally reaches the highest lattice strain values by the end of the test, except in the fine-grained ED sample.
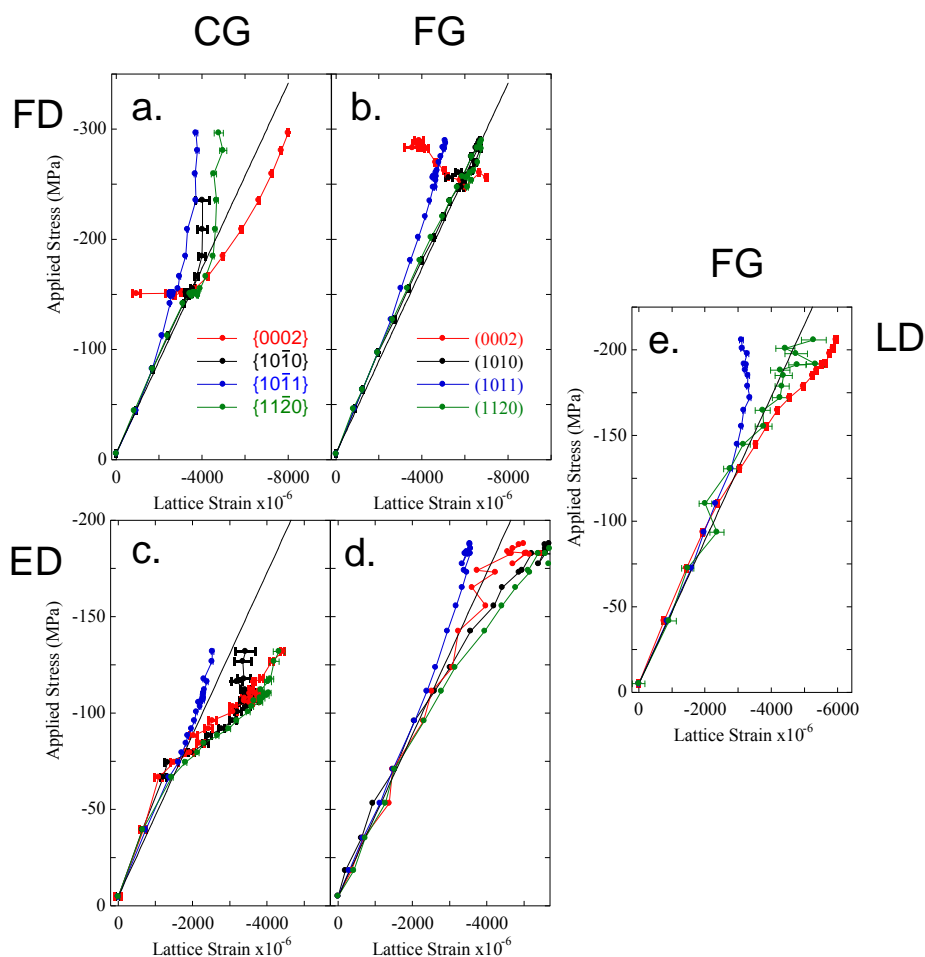
Figure 34. Applied stress versus lattice strain plots for (a) the coarse-grained material along FD, (b) the fine-grained material along FD, (c) the coarse-grained material along ED, (d) the fine-grained material along ED, and (e) the fine-grained material along LD.

Discussion

The in-situ neutron diffraction results presented here contain both straightforward

and subtle information. The crystal orientation data in Figure 33d shows that the twin

volume evolves much differently in these two materials. First, the fine-grained FD

sample has no significant twin volume until 1.5% strain, as opposed to the expected

72

immediate twinning on yield seen in the coarse-grained FD sample. Then, after twinning

begins, the twin volume growth rate reflected by the texture intensity is much lower in

the coarse-grained FD sample than the fine-grained counterpart. The less straightforward

results are from the lattice strains. Again the FD samples, shown in Figure 33a, provide

an interesting comparison. The difference in lattice strain between newly formed twins

and parents is similar, but the coarse-grained sample quickly eliminates this difference

while the fine-grained twins do not match parent lattice strain until ~8% sample

compression. Figure 34 illustrates that the spread in lattice strains during deformation

does not appear to strongly depend on grain size, inferring that the same is true for

intergranular stresses. While the lattice strains do not directly provide information about

dislocation motion, some inferences can be made. Two of these inferences are from the

relaxation of the lattices. When the $\{10\bar{1}1\}$ lattice strain trace deviates from the elastic

line in Figs 31 or 32, basal $\{0002\}$ slip is implied since it can accommodate $\{10\bar{1}1\}$

strain and has a much lower CRSS than other deformation modes that do so. Also,

relaxation of the $\{0002\}$ strain implies either pyramidal slip or twinning since these are

the only mechanisms for strain normal to the basal plane. The following sections will

rely on these assumptions to interpret the results.

Effect of Grain Size on Tensile Twinning

The twinning behavior of Mg and alloys like AZ31 is illustrated in Figure 35.

Nucleation generally occurs at grain boundaries and is immediately followed by

lengthening. Although twin formation may be energetically favorable at only six atomic

layers thick according to MD simulations [97], back-stress from the parent grain encourages growth. Using neutron diffraction and a plasticity model, Clausen et al. showed that twins will grow to at least 3% of parent grain volume immediately after nucleation as a result of the parent-twin strain mismatch [23]. This growth begins as a lengthening process that usually halts at a grain boundary, although low-angle grain boundaries are frequently crossed [98]. Ghaderi and Barnett found that for grain sizes smaller than ~30 μm, twins completely crossed a grain even at low strains (1.5%) [99]. Once this first stage of propagation is complete, twin thickening begins. As opposed to the rapid lengthening, twin thickness grows slowly as a strain-controlled process, inhibited by grain boundary pinning and the need for twin boundary dislocation climb [100]. This continues until another twin boundary is reached, the grain is consumed, or the deformation ends. While multiple twins are common in large grain sizes, their number decreases with grain size and even the coarse-grained material of this study is small enough that multiple twins are unlikely [98,99]. Further, it appears that the twin thickness just after nucleation approaches the grain width as grain size decreases [99]. In addition to these considerations, twin nucleation requires more shear stress than twin thickening [101] and more twins must be nucleated in the fine-grained material than the coarse-grained to achieve the same overall strain. Therefore, it is not surprising that twin volume growth is more difficult in the more nucleation-dependant fine-grained material than in the coarse-grained samples. There are, however, differences beyond the twin volume growth rate.

74
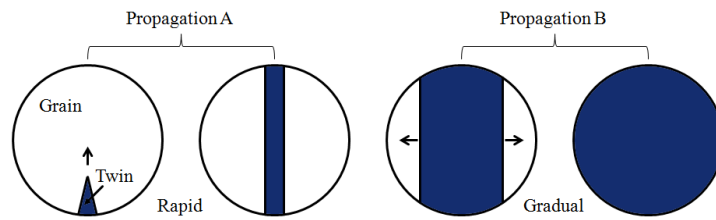
Figure 35. Nucleation and growth sequence of twins in magnesium alloys. In the samples of this study, nucleation at a grain boundary is rapidly followed by a lengthening of the twin to reach the opposing grain boundary. Strain-induced thickening follows and may consume a grain.

In the stress-strain traces obtained during deformation of the FD samples shown in Figure 30a, there is a large increase in yield strength with a decrease in grain size. In the coarse-grained sample the transition from elastic to plastic deformation is followed by a plateau, as is typical for yield by twinning. Combined with the immediate climb in $\{0002\}$ intensity in Figure 33d, it is clear that twinning is involved in the yield of the coarse-grained material. This same intensity data, however, illustrates why the stress-strain trace from the fine-grained sample departs the elastic line with more curvature; there is no evidence of twinning until 1% plastic strain and the start of twin formation is not clear until 1.5% plastic strain. This correlates with the transition to a plateau in the fine-grained FD compression trace that remains until 8% when the hardening rate begins to climb as shown in Figure 33g, entering the region marked II. The hardening rates for both fine-grained and coarse-grained samples are essentially the same in region II, and the region prior to this shows a similar rise in hardening rate. The $\{0002\}$ intensity in

75

Figure 33d, however, indicates that while the hardening rates are quite similar, the rate at which twin volume grows in the coarse-grained sample is nearly double that of the fine-grained material. Post-compression pole figures of ex-situ fine-grained FD compression samples appear almost identical to those from the coarse-grained FD samples in Figure 31, with an essentially completely twinned volume. While the fine-grained material would typically twin to a similar final intensity as the coarse-grained material during ex-situ compression to higher strain, this lower rate of twin volume growth indicates that the reduced grain size not only delays the onset of twinning but also encourages concurrent slip and twinning, as opposed to the twinning-dominated deformation for most of the coarse-grained FD compression. As both hardening curves drop after region II, the $\{0002\}$ intensity begins to level off, indicating that tensile twinning has ended. Knezevic and his colleagues have shown that this final phase is slip dominated (and would require non-basal slip) [102]. However, fracture is likely initiated by compression twinning that is expected when compressing along the c-axis at sufficient stress levels [103]. There is no clear evidence from the pole figures of compression twins but the volume fraction of these need not be large to nucleate failure. The strain accommodation in new compression twins via basal slip or double-twinning is apparently more favorable than twin growth, as observed compression twins are reported to be generally quite thin [73,104].

The $\{0002\}$ lattice strain traces in Figure 33a offer some clues to the differences in twin behavior between the two grain sizes. The initial appearance of the coarse-

76

grained $\{0002\}$ at relatively low lattice strains makes sense, as freshly nucleated twins

are typically relaxed compared to parent material [23]. While this difference may be

difficult to see in the figure, the difference in strain level between new $\{0002\}$ and parent

$\{10\overline{1}1\}$ planes is slightly higher in the fine-grained sample than the coarse-grained

sample (3000 vs 2500 $\mu\varepsilon$) so the relative relaxation of newly formed twins appears to be

influenced by grain size following the trend seen by Muransky et al [105]. However,

caution should be taken here. Given the minutes of data collection required to

confidently collect diffraction data, the observed strain levels for either study do not

necessarily correlate with the actual nucleation; observe the distinct jump in stress

between the first two $\{0002\}$ lattice strain measurements of the coarse-grained sample.

This trend could be extrapolated to a slightly lower bulk strain and was perhaps missed

in the fine-grained sample.

  While the differences in nucleation lattice strain are reported with caution, there

is a major difference in the lattice strain development: the $\{0002\}$ lattice strain

(measured from newly formed twins) in the fine-grained material does not reach the

level of the $\{10\overline{1}0\}$ lattice strain (measured from parent material) until after 10% strain,

as opposed to equalizing by 2% strain in the coarse-grained material. So, the coarse-

grained twins are quickly re-loaded, erasing their initial relaxation and eventually reach

higher levels than the parent grains. The fine-grained twins, on the other hand, are both

late to appear and to share the load. It is possible that the gradual increase in $\{0002\}$

lattice strain in the fine-grained sample is a consequence of progressive nucleation; since twins in Mg alloys tend to remain within one grain, each twin will accommodate less strain in a material with smaller grain size. Perhaps this forced further nucleation while ever-increasing stress levels were reached. However, using acoustic emission, Muransky et al. found that twin nucleation in Mg alloy was spread over a larger strain in their coarse-grained sample versus nucleating all at once in the fine-grained sample [105]. They point out that this size effect is confounded by a much larger grain size range in their coarse-grained sample and note that this spread in size could be the cause of a spread in twin nucleation. Even in the case where nucleation was spread out they saw no significant nucleation activity after <1.5% strain, the point at which the fine-grained material in the present study is just beginning to twin. For reference, their ZM20 grain sizes were 114 μm and 17 μm, much larger than the 5.5 μm and 0.78 μm AZ31 in this study. Another difference between the current results and the ZM20 study by Muransky et al. is the twin volume evolution. While their two ZM20 samples twinned at similar rates, the fine-grained samples in the present study twinned at just over half the rate of the coarse-grained samples [105]. Ghaderi and Barnett observed a grain size dependence of twin volume growth rate in Ti, but saw none in their AZ31 compression tests [99]. Since their smallest grain size was almost the same as the coarse-grained material in this study, this may be another indication of a critical grain size rather than a size-dependent trend. However, similar to the present results, Jain et al. saw a decrease in twin volume growth rate with decreasing grain size in AZ31 tensile tests [73]. Although they speculated that weakened texture due to heat treatment (in order to produce large grain

78

sizes) was the cause, it may be that twin volume growth rate is dependent on grain size even in coarse material in tension testing.

Another study showed the effect of grain size on the activation of twinning without the aid of neutron diffraction [92]. Barnett and his colleagues varied temperature during tensile testing knowing that the critical resolved shear stress ratios between different systems decreases with increasing temperature and, most relevantly, deformation will transition from twinning to slip at elevated temperatures [92]. They showed that reduced grain size can restrain twin formation using a careful interpretation of the mechanical response combined with orientation imaging microscopy observations. Further, they also argued that there is a critical grain size at which a sharp change in behavior takes place. Barnett later refined this argument on the basis of twin number density (per volume) increasing with decreasing grain size [106]. The implication that this would be true at room temperature given a small enough grain size has been supported here.

<center>*Effect of Grain Size and Texture on Slip*</center>

The ED compression samples are expected to rely almost entirely on basal slip for both the yield mechanism and the presented plastic deformation. There is a minor grain population oriented with basal poles perpendicular to the compression axis but the stress levels during compression do not reach the yield values of the corresponding FD samples, so it is not expected that twins would be initiated in these perpendicular grains (and unobserved). Since both the ED samples yielded by the same mechanism, these samples should demonstrate the grain size effect on basal slip alone, as opposed to the

<center>79</center>

FD samples where the samples yielded by different mechanisms. While only one size is studied in the LD direction, the LD fine-grained sample does provide some insight on the effects of minor texture components when compared to the ED fine-grained material. The two major $\{0002\}$ peaks are still positioned such that basal slip is favored in most grains. However, the weak "bridge" between the peaks is now aligned with the compression axis (as seen in Figure 31), which implies that non-basal slip and compression twinning will be more active. Evidence for compression twin formation in the LD sample can be seen when comparing the ED and LD intensities in Figure 33e and f. The $\{0002\}$ intensity begins to slowly climb in the ED samples as the basal poles rotate towards the compression axis. In the LD sample, on the other hand, this intensity remains essentially flat, indicating that some mechanism is reorienting some of the grains away while basal slip reorients more basal plates towards the compression axis. As basal poles rotate toward the compression axis, non-basal slip or compression twinning would be required to continue deformation. As implied by the flat $\{10\overline{1}1\}$ lattice strains (Figure 33b and c), grains still undergoing basal slip in the ED and LD samples do not harden during the test, so not enough stress is applied to trigger pyramidal slip or compression twinning in the grains rotated towards the test axis. Without a relaxation method, this should result in an increase in the $\{0002\}$ lattice strain, which in fact is seen in Figure 33b and c. The hardening observed in the macro stress-strain curves of Figure 30b and c is therefore attributable only to elastic strain in the

80

grains being reoriented with their {0002} poles along the compression axis rather than a hardening of the basal slip due to dislocation interactions.

Turning to the different representation in Figure 34, another observation can be made. The ED compression samples in Figure 34c and d contain more diffraction traces but are somewhat simpler than their FD counterparts. The lattice strains depart the elastic line simultaneously in both samples as one would expect for a continuous transition from elastic to plastic deformation via one slip mechanism. While the lattice strains in the coarse-grained sample may appear to spread more quickly than the fine-grained material in this presentation, this is an effect of the much higher stress reached by the fine-grained material. In fact, the spread is nearly the same at the end of the two tests. This implies similar intergranular stresses in the two samples despite a significant difference in strength.

After this study was completed, my colleague SM Razavi conducted a thorough study of AZ31 under the guidance of I. Karaman that further elucidated the impact of grain size on slip in this alloy. Figure 36 is a key result of her work and is from her Master of Science thesis [55]. Clearly, yield by basal slip has a much lower Hall-Petch constant at room temperature than tensile twinning, reaffirming the results of this study. Interestingly, prismatic slip was also shown to be much more sensitive to grain size than basal slip. Her works [55,57] are recommended reading for those wishing to learn more about grain size effects on deformation or ECAE processing of anisotropic materials.
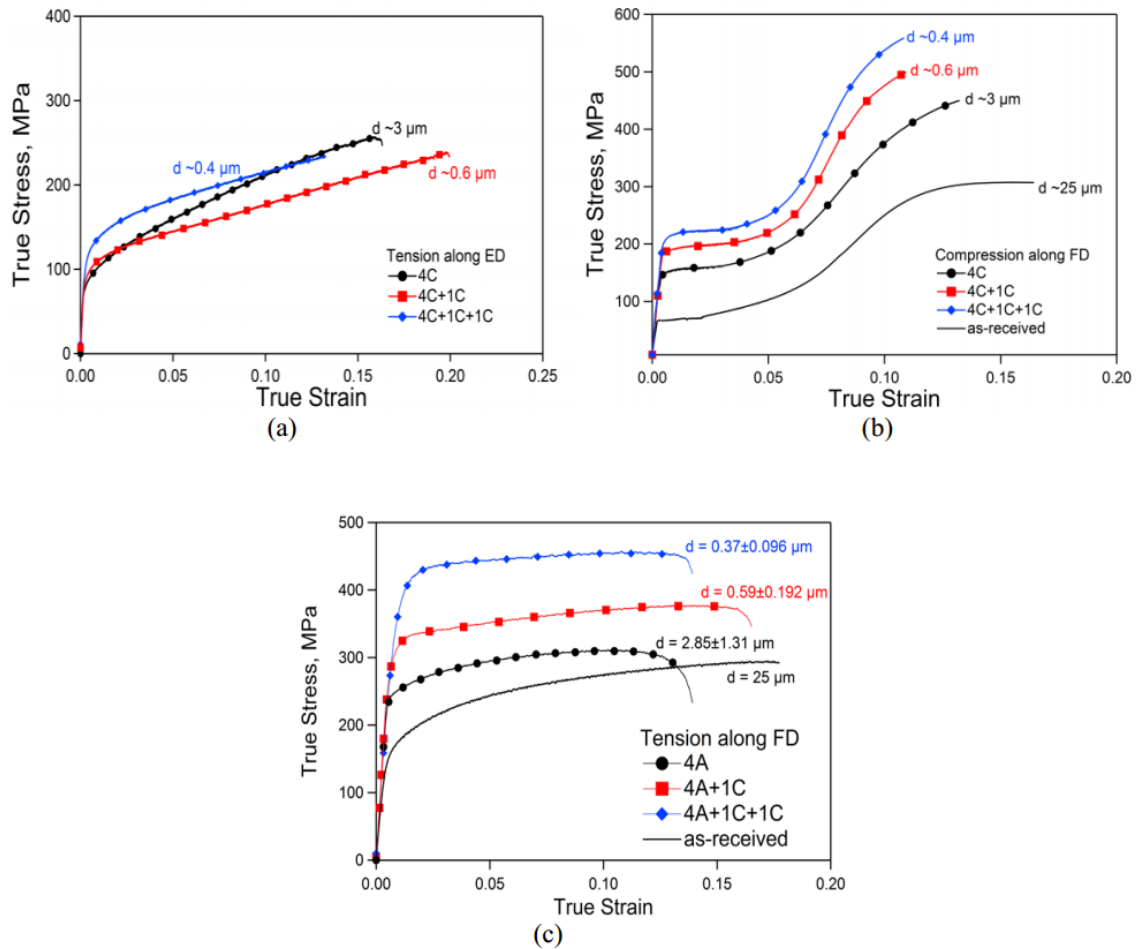
Figure 36. Impact of grain size on mechanical response under (a) basal slip, (b) tensile twinning, and (c) prismatic slip [55].

Conclusions

This work examined the behavior of AZ31 magnesium alloy with micron and sub-micron grain sizes, differing by almost an order of magnitude, but with comparable crystallographic textures. By measuring the lattice strains under loading in several orientations as well as the texture evolution, the effects of grain size on twin nucleation and twin volume growth were established. The following conclusions should be

82

applicable to Mg alloys as a material class generally and the common AZ alloys specifically.

1. Tensile twin nucleation is grain size dependent. That is, there is a grain size below which slip will become the room temperature yield mechanism instead of twinning in crystallographic textures oriented to encourage twinning. That grain size appears to be near 1 μm in AZ31 magnesium alloy. Twin nucleation was delayed until 1.5% plastic strain in the fine-grained (0.78 μm) material of this study.

2. Twin volume growth was shown to be strongly dependent on grain size. Twin volume in the fine-grained material grew at a slightly over half the rate of the coarse-grained material. This difference is attributed to progressive twin nucleation in the fine-grained material rather than diffuse nucleation followed by growth in the coarse-grained material.

3. Intergranular stress does not appear to be affected by grain size.

4. The twin-parent strain mismatch immediately after twin nucleation is confirmed to be grain size dependent.

CHAPTER IV

DESIGNED TEXTURE VIA THERMOMECHANICAL PROCESSING

Introduction

While the range of mechanical anisotropy produced by our grain refinement

oriented work in Chapter II was significant, we chose to address other related questions.

The relatively weak texture generated by Route B_c leads to low mechanical anisotropy

and the hybrid routes lead to high anisotropy. If these extremes could be expanded, it

would improve performance and broaden the alloy's applicability while increasing our

knowledge of its deformation behavior. Mechanically isotropic magnesium may not be

achievable using deformation. Even casting, which can result in random texture in the

core of a large casting [107] exhibits preferred orientation near surfaces due to the

tendency for close-packed planes to form along the liquid-solid interface [108].

Consolidation of powder by spark plasma sintering may be the only currently available

method to generate a randomly textured submicron grain sized material with

conventional alloys [109]. Materials with high mechanical anisotropy, on the other hand,

are desirable for cutting-edge structures in applications from tissue engineering [110] to

vehicle design [111]. One other key aspect limiting magnesium alloy applications, poor

corrosion performance in many alloys, is also sensitive to texture. The basal planes have

a much lower electrode potential than other orientations, leading to significant changes

in corrosion rate depending on texture and orientation [112]. By tailoring the texture of

wrought product to strongly align the basal planes with susceptible surfaces, corrosion

rate and pitting susceptibility can be reduced dramatically. Given the appropriate process

optimization, wrought magnesium alloys could also outperform other structural materials for advanced applications requiring unique property combinations not currently available. In this chapter we will demonstrate that, building on knowledge from the previous two chapters, we can control both texture intensity and orientation.

Materials and Methods

The hot rolled plate used for the starting material in this study was from a different batch than that used in Chapter II and Chapter III. The ECAE tooling and characterization methods, however, are shared with Chapter II. Additional processing was conducted using an International Rolling Mills heated rolling mill with 13cm roll diameter. This was used to roll material from room temperature to 150°C. Heating rolling steps were conducted by removing the workpiece from a co-located oven and inserting into the moving rolls within five seconds. Rolling was conducted at 2mm/s and rolling reductions were 2-4% per pass. Thickness was recorded between each pass using dial calipers prior to reinsertion in the oven for 8 minutes. An additional characterization method, electron back scatter diffraction (EBSD) was employed using an accelerating voltage of 20 kV, beam current of 5 nA and 70° stage tilt. EBSD was performed by Lisa Chan of EDAX.

Results and Discussion

Strengthening ECAE Texture

Having established that temperature step-down ECAE processing can create UFG microstructures, we focused on texture intensity. After attempting several versions of low temperature routes and knowing that, as indicated by Table 1, non-basal slip

becomes much more difficult as temperature drops, our path forward was clear. Using the same hybrid route approach at higher temperatures, we would finish the processing with repeated low-temperature route C to preferentially activate basal slip. Repeatedly shearing the material on the same plane allowed us to take advantage not only of a specific deformation condition, but also of the limited slip directions. Since basal slip is parallel to the prismatic faces, cycling the deformation on one plane and one direction leads to a highly oriented material when compared to the ECAE processed material in Chapter II. Figure 37 is an optical micrograph and texture of AZ31 that has been processed 26H: $3B_c$ at 200^oC + 1C at 200^oC + 2C at 150^oC + 1C at 125^oC + 1C at 100^oC. This processing results in a strong texture; notice the three peaks in the $(10\bar{1}0)$ pole figure, corresponding to the three prismatic planes of a single crystal. In addition, the (0002) pole figure is highly concentrated. We refer to this texture as "quasi-single-crystal" since it is a slightly weakened version of a perfect single crystal.
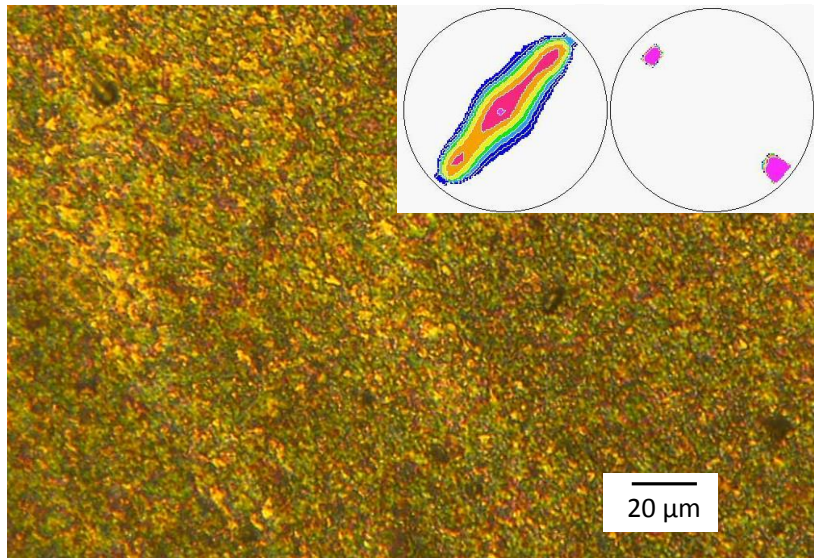
Figure 37. Optical micrograph with prismatic and basal texture of AZ31 material 26H taken from the flow direction. 26H was ECAE processed 3B$_c$ at 200°C + 1C at 200°C + 2C at 150°C + 1C at 125°C + 1C at 100°C.

EBSD was undertaken to better characterize the microstructure of the 26H material. Figure 38 compares the inverse pole figure (IPF) maps of the initial rolled plate (plate normal) and the processed material (flow plane with view rotated to center on the texture peak for comparison). Notice that the scale bars are dramatically different. The EBSD measurements indicate that the plate has an average grain size of 18 μm while the processed 26H material has an average grain size of 0.17 μm, a full two orders of magnitude in grain size reduction. However, some caution is advised when observing these results. First, the smaller grains are tilted far from the large grains, and such a significant fraction of the material so oriented should appear in the XRD pole figure in Figure 37. Since it does not, we must assume that these regions have sufficiently high dislocation concentrations to interfere with Kikuchi pattern interpretation. Indeed, the

87

corresponding confidence index maps in Figure 39 highlight this problem. So, while

EBSD indicates an exceptionally small average grain size, if we ignore the low end the

average grain size from EBSD is ~0.3 μm.
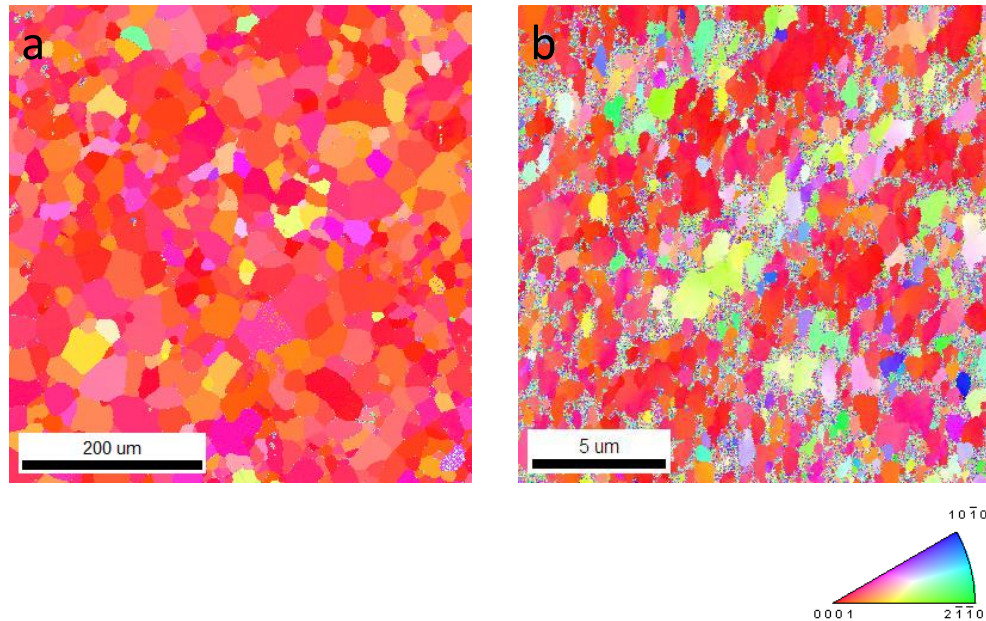
Figure 38. EBSD generated IPF maps of AZ31B in a. hot rolled and b. 26H conditions. 26H was processed 3B$_c$ at 200°C + 1C at 200°C + 2C at 150°C + 1C at 125°C + 1C at 100°C.

	Min	Max	Total Fraction
	0	0.2	0.311
	0.2	0.4	0.027
	0.4	0.6	0.042
	0.6	0.8	0.105
	0.8	1	0.514

Figure 39. Confidence index maps of AZ31B in a. hot rolled and b. 26H conditions. 26H was processed $3B_c$ at 200^oC + 1C at 200^oC + 2C at 150^oC + 1C at 125^oC + 1C at 100^oC.

The mechanical response of the strongly textured material is unsurprisingly anisotropic. Just as significant as the differences in yield strength along different directions, however, is the increase compared to the starting material. While the weaker texture of the hot rolled plate certainly plays a roll, two loading conditions seem similar between the samples. The in-plane (TD) direction of the rolled plate, parallel to most basal planes, is similar to the flow direction in the processed material in that tensile twinning should be activated. Similarly, the through-thickness plate and 47° bar samples are both along the basal poles, as depicted in Figure 40. In the case where twinning is encouraged, yield strength more than doubles after processing. Yield strength in the case

of compression along the c-axis almost quadruples. Part of the large difference between the ND-FD pair is that some of the more favorably oriented grains in the hot rolled plate will yield by basal slip during through-thickness (ND) compression, while basal slip is completely inactive in the 26H sample. When samples are oriented to ensure yield by basal slip, as in Figure 41, the differences are much more modest, highlighting the low grain size sensitivity of basal slip [55]. The 26H processing has created an AZ31 material with a compression anisotropy ratio of 5:1, surpassing our expectations at the start of the project.
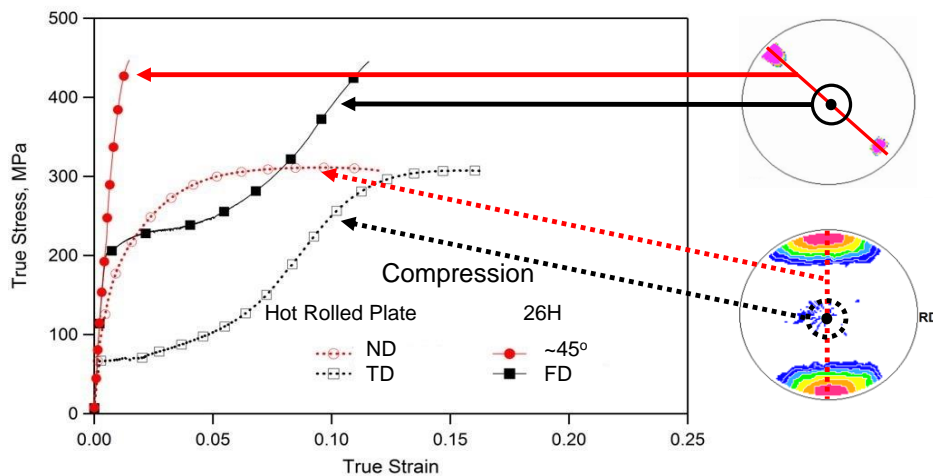
Figure 40. Compressive response and basal pole figures for orientation reference of AZ31 in hot rolled and 26H conditions. 26H was processed $3B_c$ at 200^oC + 1C at 200^oC + 2C at 150^oC + 1C at 125^oC + 1C at 100^oC.
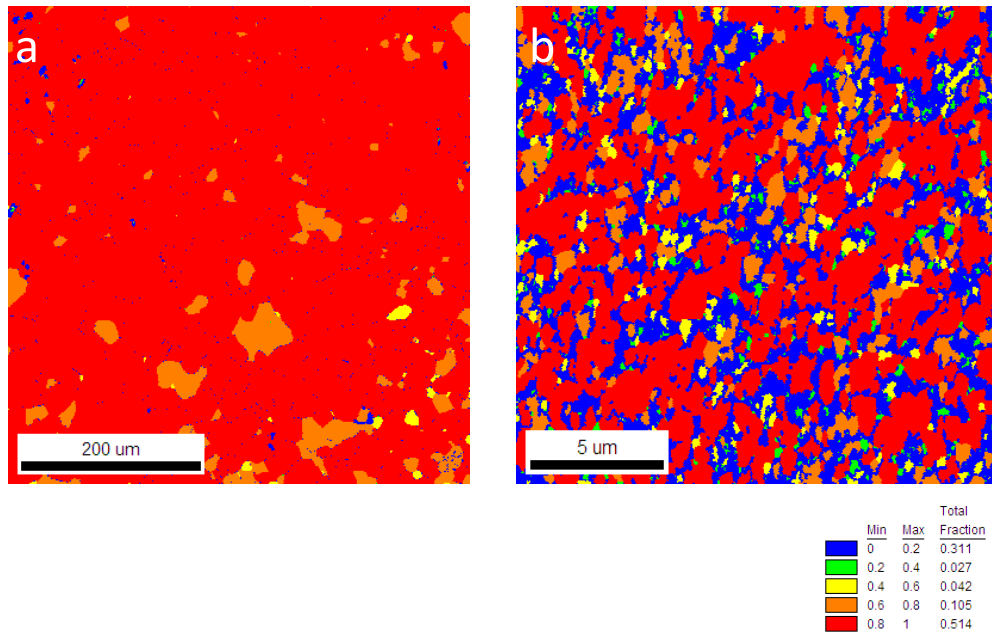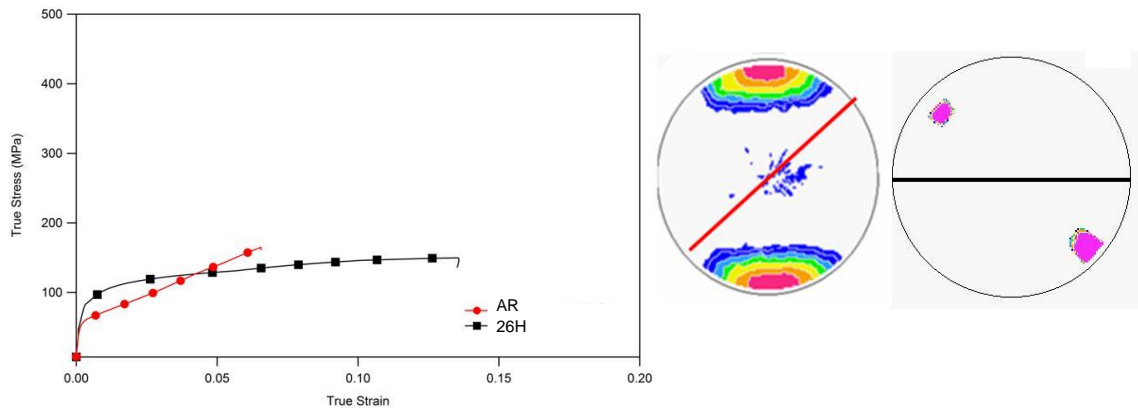
Figure 41. Compressive response with basal pole figures of AZ31 in hot rolled and 26H conditions. Orientation of compression axis, as indicated on pole figures, is intended to maximize basal slip. 26H was processed 3B$_c$ at 200°C + 1C at 200°C + 2C at 150°C + 1C at 125°C + 1C at 100°C.

The impact of texture strength is a significant contributor to the mechanical response of 26H. The FD compression response of 26H activates tensile twinning as expected, but there is an unexpected difference when compared to the FD response of 5H in Figure 11. Although the grain sizes are similar, the yield strength of 5H is 50% higher than 26H. While we demonstrated in Chapter III that tensile twin activation is not only dependent on, but can be suppressed by grain size, this requires that the twin formation depicted in Figure 35 begins and ends in a single grain. Beyerlein and her colleagues showed that low-angle grain boundaries are frequently crossed by twins [98]. Given the strong basal and non-basal texture in AZ26, low-angle boundaries are expected to be frequent so it is not surprising that the effective grain size inhibiting twin formation appears to be close to 0.5 µm. This also factors into the brittle response of the 47° compression in 26H; the fracture-inducing action of compressive and double-

twinning is encouraged by the larger apparent grain size. This microstructural character is not indicated by the ECAE processing literature. Conventionally, additional passes result in an increased fraction of high angle grain boundaries [113]. As temperature is reduced in AZ31, however, the CRSS ratios encouraging basal slip alone begin to eliminate these high angle grain boundaries. In fact, an attempt to further sharpen the texture using an all-C-route temperature step-down approach takes the low-angle grain boundary appearance to a new level.

Grain Growth via Low Temperature ECAE

In an attempt to further sharpen the texture of AZ31 using ECAE, additional Route C processing was utilized. The 32H route consists of 4C at 200°C + 1C at 150°C + 1C at 125°C + 2C at 100°C. This is a similar process to 26H with the encouragement of slightly more basal slip. The processed AZ31 has the texture shown in Figure 42. Although this texture is slightly weaker than the 25H texture, the impact of large shear deformation under limited slip conditions on the microstructure is dramatic. Figure 43 compares low and high magnification micrographs of 5H and 32H samples from the flow plane. The streaks from the upper left to lower right in the low-magnification 32H micrograph are not indicative of the microstructure but are an artifact of the polishing process. In a cubic material, the additional strain undergone during 32H would result in a microstructure that was at least as refined as the 5H. In the case of HCP-structured AZ31, the initially refined microstructure has undergone reorientation and recombination during the final low-temperature passes, growing the grains dramatically. This is an extension of the behavior of the 26H material, as the alignment of neighboring

grains leads to lower grain boundary angles and finally the coalescence of these

neighbors. The grain refinement by ECAE that was a primary goal in the work of

Chapter II seems limited by this phenomenon; the limited availability of non-basal slip

below ~125°C requires Route C processing, but repeated C processing leads to grain

growth rather than grain refinement.
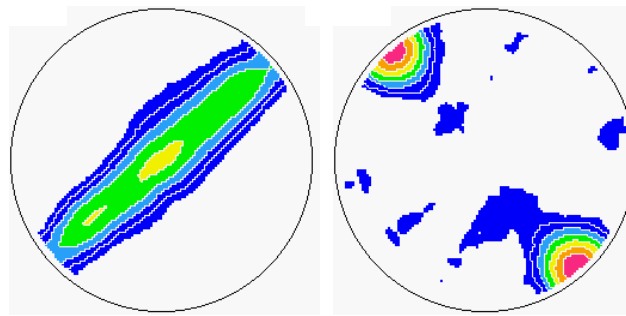
Figure 42. Prismatic and basal texture of AZ31 in 32H condition after ECAE processing 4C at 200°C + 1C at 150°C + 1C at 125°C + 2C at 100°C.

Figure 43. Low magnification secondary electron micrographs of AZ31 processed (a) 5H (2A at 200°C + 1C at 150°C + 1A at 150°C + 1C at 125°C) and(b) 32H (4C at 200°C + 1C at 150°C + 1C at 125°C + 2C at 100°C) and high magnification of (c) 5H and (d) 32H.

Textures Control via ECAE + Rolling

Some applications of magnesium alloy may be best served by the C-type texture

produced by the low temperature routes. This texture maximizes extension in one

direction. However, many applications where anisotropic properties are desirable require

that in-plane properties are uniform. Additionally, applications for sheet and plate such

as armor often require maximized through-thickness compression strength or in-plane tension strength. With this in mind, we would like to create a material with small grain size and a sharper version of the hot rolled plate texture, aligning the c-axis with the plate normal. There are several approaches to this goal; we chose to pursue ECAE followed by rolling as a method to grain refine the material and then optimize its texture.

Since the discussion in this chapter began with 26H processing, it is illustrative to characterize the effects of rolling on that material. Figure 44 portrays the basal pole figures from the LD/plate normal before and after rolling the ECAE-processed material at room temperature. The sample was rolled to a 30% rolling reduction at room temperature, at which point cracks developed and the back of the rolled piece separated from the rest of the material. The transformation of the basal texture is depicted in Figure 44. The peak intensity has rotated towards the plate normal, but has not reached the desired central position. Instead, after scaling the pole figure to highlight weak texture intensity, the presence of compression twins is indicated; the two peaks are separated by 54°, essentially the 56° reorientation after compression twinning. While the presence of sufficient compression twin volume to appear in XRD data was surprising, the difficulty with rotating this texture was not. However, there were alternatives.

Now looking at pole fig from top surface (plate convention)

Surface Cracks develop

30% Rolling Reduction

ED/ RD

Compression twinning indicated
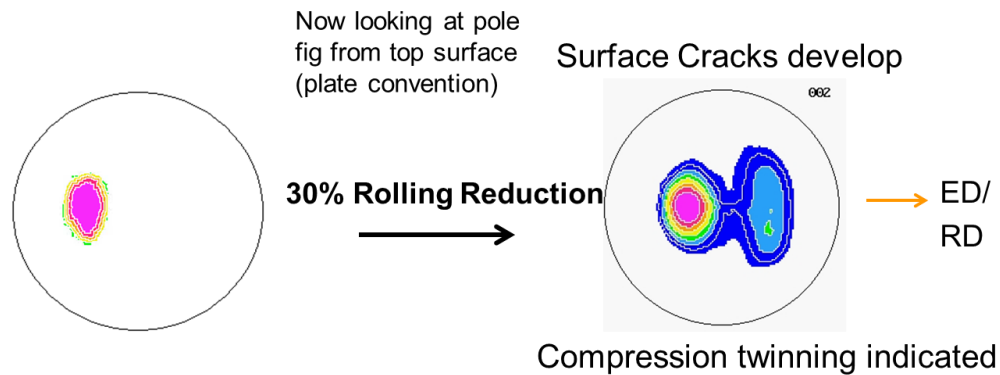
Figure 44. Rolling plane basal pole figures of AZ31 processed 26H and rolled in the extrusion direction at room temperature to a 30% thickness reduction (thickness in LD direction). Pole figures taken from plate normal before and after rolling.

Attempting rolling reduction at an elevated temperature would increase the availability of non-basal slip and perhaps delay the onset of compression twinning. The 26H material was rolled at 100°C to a rolling reduction of 51% before surface cracks appeared. At this point the peak was 20° from center, as shown in Figure 45. Rolling at 150°C resulted in a 69% reduction before cracks appeared but the peak was still 15° from the plate normal. Further elevating the rolling temperature would encourage dynamic recrystallization, consuming the microstructure and negating the low temperature processing. Although the strong texture and submicron grain size of 26H was desirable, it was apparent that another path must be sought.
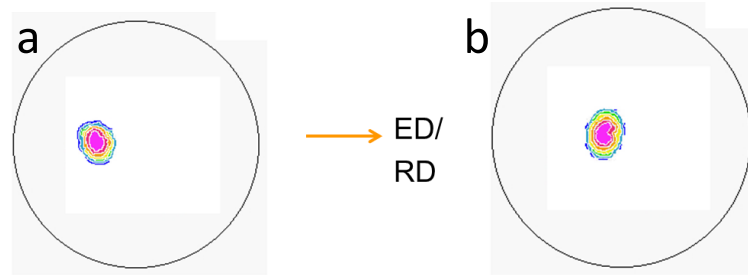
Figure 45. Basal pole figures of AZ31 processed 26H (3B$_c$ at 200°C + 1C at 200°C + 2C at 150°C + 1C at 125°C + 1C at 100°C) and then reduced by rolling in the LD direction until surface cracks were noted at (a) 100°C and (b) 150°C.

To set a baseline, the coarse grain hot-rolled plate was sectioned at a 45° angle and rolled to a 54% reduction at 150°C. This resulted in the desired centering of the basal poles around the plate normal, as shown in in Figure 46. Knowing that such a reorientation was possible at elevated temperature was encouraging, and other rolling attempts were made using C-type texture materials. It appears, however, that the peak reorientation is limited by refined grain size, as the hybrid route materials suffered from cracking long before reorienting. Even the micron-sized microstructures were resistant. The 4-5 µm average grain size material that was ECAE processed 4C at 200°C was successfully rolled to 35% reduction, resulting in an alignment of the secondary peak with the plate normal but a 27° tilt in the main peak. The limited capacity for rotating the texture of a fine-grain material using this method was clear.
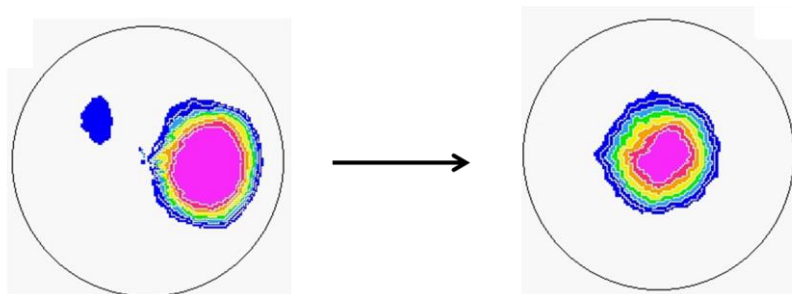
Figure 46. Basal pole figures of AZ31 hot rolled plate material sectioned at a 45$^{\text{o}}$ angle and rolled at 150$^{\text{o}}$C. Pole figures taken before and after rolling.

An alternative to rotating a C-type texture is strengthening an A-type texture. Again looking to the DRX-refined materials, AZ31 processed 4A at 200$^{\text{o}}$C was reduced by 30% at 150$^{\text{o}}$C to sharpen and reorient the texture. The basal textures before and after rolling are depicted in Figure 47. The peak intensity is still 6$^{\text{o}}$ from plate normal but the texture is nevertheless quite close to the goal of an intensified rolled plate character with the advantage of a refined microstructure.
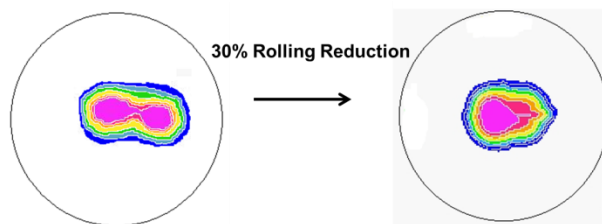
Figure 47. Basal pole figures of AZ31 processed by 4A at 200$^{\text{o}}$C followed by a 30% rolling reduction. Pole figures taken before and after rolling.

A simple measure of the effectiveness of this texture reorientation via rolling is the change in the yield strength along the extrusion/rolling direction. As the basal poles reorient away from this direction towards the rolled plate normal, the strength should increase due to the inactivation of basal slip. Three such cases are presented in Figure 48. The 4C and 4A materials are typical of their texture type, while the hybrid route plate material marked A10 has a split texture between the ideal A or C texture types. The impact of rolling these materials at 150°C can be evaluated from two viewpoints. The 4A material started and finishes with the highest yield, so this processing methodology may be the best approach for obtaining a plate or sheet product with desired mechanical property optimization. However, the impact of rolling is more dramatic on the materials with a C-type texture component. The yield strength increase in the 4C case is approaching double the initial strength and highlights the impact of texture reorientation by rolling.

Strengthen "A" Textures

	Initial Yield (MPa)	Afer 150°C Rolling (MPa)	Increase (%)
4A@200°C	210	255	21
Hybrid A10	150	200	33
4C@200°C	90	160	78

Rotate "C" Textures
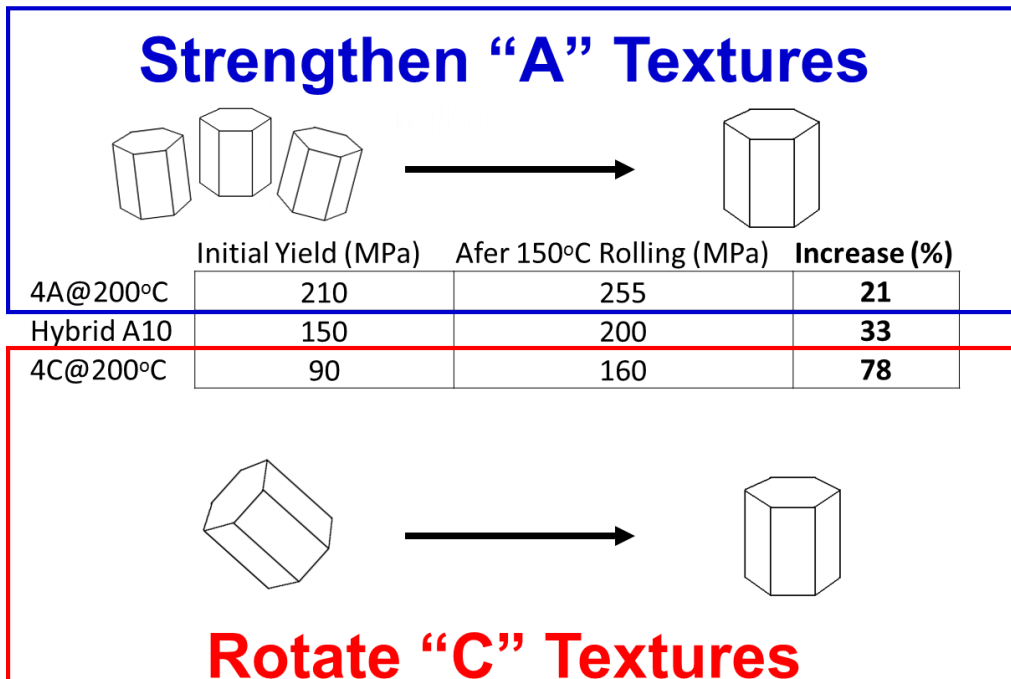
Figure 48. Impact of warm rolling on ED/RD tensile yield strength of ECAE-processed AZ31.

Having established that severe plastic deformation can significantly alter the mechanical response of AZ31 under typical room temperature mechanical testing conditions, a final note concerning the properties under different conditions is of interest. Plates were processed via hybrid routes to generate material as in Figure 20 and Figure 21. These plates were tested for ballistic impact response at the US Army research lab. Unfortunately, in this case testing indicated that ECAE processed plates performed only slightly better than commercial plate when tested against a 0.17in fragment simulating projectile threat [114]. The Texture A plate at 0.482in thick had a V_{50} of 2117fps versus the AR at 2046fps. The Texture C plate at 0.462in thick had a V50 of 2070fps versus the

AR at 1967fps. The marginal, ~5% improvement is partially due to the dimensional similarity between the incoming round diameter and the plate thickness. However, it also signals inherent properties of the material under high strain rate that grain refinement is unable to change. The suitability of magnesium alloys for withstanding high-strain-rate events, such as automobile crashes, has long been in question [110].

Conclusions

There are applications of magnesium alloy that would benefit from anisotropic mechanical properties tailored for the specific requirements of the component. ECAE + rolling can generate desirable anisotropy in AZ31B by taking advantage of texture reorientation during warm rolling. High unidirectional strengths (400MPa yield) are achievable in this alloy under certain conditions using ECAE processing with sufficient strain along essentially one axis, under conditions promoting only basal slip. This method relies on the limited independent slip systems in AZ31 at lower temperatures, leading to strong orientation followed by grain growth. While the resulting microstructures may result in limited improvement to high-strain response, the optimized mechanical properties provide an alternative to weakly textured material for applications with high load requirements in specific orientations.

CHAPTER V

CONCLUSIONS

Equal channel angular extrusion combined with other thermomechanical processing is a viable method for generating magnesium alloy material with high mechanical performance. This processing requires a broad and deep knowledge of Mg deformation under a wide range of conditions. We have contributed to this knowledge and utilized it to create AZ31 alloy material with extreme textures and microstructures, and mechanical performance.

Our accomplishments include:

1. The development of a range of hybrid ECAE routes that generate AZ31 with a variety of textures and a wide range of grain sizes.

2. The inhibition of yield by tensile twinning utilizing refined grain size.

3. Demonstration of the capability of plate ECAE to replicate bar processed product while also permitting a new strain path.

4. The use of ECAE + Rolling to enhance unidirectional strength.

5. Created quasi-single-crystal texture using ECAE

The wide range of mechanical properties demonstrated in a single alloy illustrates the power of a carefully designed thermomechanical processing strategy. By providing methods to reach yield strengths up to 400MPa and 5:1 yield anisotropy in a relatively low-strength alloy, this work lends a framework to materials engineers seeking to maximize the performance of wrought magnesium products.

Future Work

In order to expand on this work and further the general effort to improve magnesium alloy properties, a few avenues of study and development are offered. While we chose to focus on the solid-solution-strengthened AZ31 alloy, a closer examination of the ZK60 alloys would be beneficial. A thorough understanding of the temperature dependence of deformation modes in this alloy may result in a thermomechanical processing design that exceeds 350MPa yield strength while maintaining the nearly isotropic yield demonstrated by one case in the current work. In order to further enhance strength and reduce anisotropy, however, a more advanced heat treatable alloy must be developed. This alloy would form a uniformly distributed set of precipitates with geometry, orientation and coherence such that basal slip is preferentially inhibited. The suppression of twin growth and perhaps twin nucleation are also desirable. Using a combination of precipitate types may result in a dramatic drop in mechanical anisotropy even before a well-designed thermomechanical process comes into play [115].

Adding particles to the casting could significantly impact strength and anisotropy in Mg alloys. We performed some preliminary work on graphene-containing Mg alloys in collaboration with Xiaochen Li and his postdoc Lianyi Chen. The initial results demonstrated that ECAE could solve some of the issues with this material and resulted in the distribution and alignment of the graphene while eliminating porosity. Since ECAE can be used to tailor microstructural morphology as well as texture, we anticipate significant control over mechanical behavior. While follow-up was limited at the time, this appears to be a fundable and fertile area of future pursuit.

REFERENCES

[1] H.E. Friedrich, B.L. Mordike, Magnesium Technology : Metallurgy, Design Data, Applications, Springer, Berlin, 2006.

[2] H.A. Klagsbrunn, Ind Eng Chem, 37 (1945) 608-617.

[3] S. Ramakrishnan, P. Koltun, Resour Conserv Recy, 42 (2004) 49-64.

[4] D. Eliezer, E. Aghion, F.H. Froes, Adv Perform Mater, 5 (1998) 201-212.

[5] Datasheet 462. Magnesium Elektron UK, Manchester, UK, 2005.

[6] P.D. Caton, in: B.L. Mordike, K.U. Kainer, Magnesium Alloys and Their Applications, Werkstoff-Informationsgesellschaft, 1992, Wolsburg, Germany, p. 367-373.

[7] "Metal Prices", InvestmentMine, Web, 20 April, 2014.

[8] A.J. Baime, Go like hell : Ford, Ferrari, and their battle for speed and glory at Le Mans, Houghton Mifflin Harcourt, Boston, 2009.

[9] M. Liu, D.S. Shih, C. Parish, A. Atrens, Corros Sci, 54 (2012) 139-142.

[10] A. Prasad, Z.M. Shi, A. Atrens, Corros Sci, 55 (2012) 153-163.

[11] E.A. Nyberg, A.A. Luo, K. Sadayappan, W.F. Shi, Adv Mater Process, 166 (2008) 35-37.

[12] J. Gann, Soc Automotive Eng Trans, 30 (1931) 620.

[13] Datasheet 482, Magnesium Elektron UK, Manchester, UK, 2005.

[14] Datasheet 102, Magnesium Elektron UK, Manchester, UK, 2008.

[15] Datasheet 1380e, Aubert & Duval, Paris 2011.

[16] Creusabro 8000, Abraservice UK, Birmingham, UK, 2011.

[17] Technical Data Sheet ATI Ti-6Al-4V, Allegheny Technologies Inc., Pittsburg, PA, 2012.

[18] Aluminum standards and data 2009, The Aluminum Association, Arlington, VA, 2009.

[19] T.A. Rickard, J R Anthropol Inst G, 71 (1941) 55-56.

[20] J.A. Charles, Am J Archaeol, 71 (1967) 21-26.

[21] C.H. Cáceres, D.M. Rovera, J Light Metals, 1 (2001) 151-156.

[22] A. Jain, S.R. Agnew, Mat Sci Eng A, 462 (2007) 29-36.

[23] B. Clausen, C.N. Tomé, D.W. Brown, S.R. Agnew, Acta Mater, 56 (2008) 2456-2468.

[24] D. Ando, J. Koike, Y. Sutou, Mater Sci Eng A, 600 (2014) 145-152.

[25] A. Levinson, R. Mishra, R. Doherty, S. Kalidindi, Metall and Mat Trans A, 43 (2012) 3824-3833.

[26] B. Kondori, A.A. Benzerga, Metall and Mat Trans A, 45 (2014) 3292-3307.

[27] A. Jäger, P. Lukáč, V. Gärtnerová, J. Bohlen, K.U. Kainer, J Alloy Compd, 378 (2004) 184-187.

[28] D. Ponge, G. Gottstein, Acta Mater, 46 (1998) 69-80.

[29] Y. Miyahara, K. Matsubara, Z. Horita, T. Langdon, Metall and Mat Trans A, 36 (2005) 1705-1711.

[30] J. Koike, T. Kobayashi, T. Mukai, H. Watanabe, M. Suzuki, K. Maruyama, K. Higashi, Acta Mater, 51 (2003) 2055-2065.

[31] V.M. Segal, R.E. Goforth, K.T. Hartwig, in: H. Heinin, T. Oki (eds.), First International Conference on Processing Materials for Properties, Honolulu, (1993) 971-974.

[32] D.C. Foley, R.E. Barber, J.T. Im, B. Onipede, K.T. Hartwig, Mater Sci Forum, 584-586 (2008) 63-67.

[33] R.Y. Lapovok, J Mater Sci, 40 (2005) 341-346.

[34] R. Lapovok, L.S. Tóth, A. Molinari, Y. Estrin, J Mech and Phys Solids, 57 (2009) 122-136.

[35] A. Yamashita, Z. Horita, T.G. Langdon, Mater Sci Eng A, 300 (2001) 142-147.

[36] S.R. Agnew, P. Mehrotra, T.M. Lillo, G.M. Stoica, P.K. Liaw, Acta Mater, 53 (2005) 3135-3146.

[37] S.X. Ding, W.T. Lee, C.P. Chang, L.W. Chang, P.W. Kao, Scripta Mater, 59 (2008) 1006-1009.

[38] X.M. Feng, T.T. Ai, Trans Nonferr Metal Soc, 19 (2009) 293-298.

[39] B. Chen, D. L. Lin, L. Jin, X. Q. Zeng, C. Lu, Mater Sci Eng A, 483–484 (2008) 113-116.

[40] T. Mukai, M. Yamanoi, H. Watanabe, K. Ishikawa, K. Higashi, Mater Trans, 42 (2001) 1177-1181.

[41] H.K. Kim, W.J. Kim, Mater Sci Eng A, 385 (2004) 300-308.

[42] S. Biswas, S. Singh Dhinwal, S. Suwas, Acta Mater, 58 (2010) 3247-3261.

[43] M. Al-Maharbi, I. Karaman, I.J. Beyerlein, D.C. Foley, K.T. Hartwig, L.J. Kecskes, S.N. Mathaudhu, Mater Sci Eng A, 528 (2011) 7616-7627.

[44] W.J. Kim, J.B. Lee, W.Y. Kim, H.T. Jeong, H.G. Jeong, Scripta Mater, 56 (2007) 309-312.

[45] S.R. Agnew, Ö. Duygulu, Int J Plasticity, 21 (2005) 1161-1193.

[46] J.C. Tan, M.J. Tan, Mater Sci Eng A, 339 (2003) 124-132.

[47] M. Kamachi, M. Furukawa, Z. Horita, T.G. Langdon, Mater Sci Eng A, 361 (2003) 258-266.

[48] C. Xu, T. Langdon, Z. Horita, M. Furukawa, J. of Mater Eng and Perform, 13 (2004) 683-690.

[49] O.V. Mishin, V.M. Segal, S. Ferrasse, Metall Mater Trans A, 43A (2012) 4767-4776.

[50] M. Furukawa, Z. Horita, T.G. Langdon, Mater Sci Eng A, 332 (2002) 97-109.

[51] M.R. Barnett, J Light Metals, 1 (2001) 167-177.

[52] M.H. Al Maharbi, I. Karaman, G. Purcek, Mater Sci Eng A, 527 (2010) 518-525.

[53] M.H. Al Maharbi, I. Karaman, Adv Mater Res, 911 (2014) 178-184.

[54] S.R. Agnew, C.N. Tomé, D.W. Brown, T.M. Holden, S.C. Vogel, Scripta Mater, 48 (2003) 1003-1008.

[55] S.M. Razavi, Thesis, Texas A&M University, College Station, TX, 2011.

[56] M.H. Al Maharbi, Dissertation, Texas A&M University, College Station, TX, 2011.

[57] S.M. Razavi, D.C. Foley, I. Karaman, K.T. Hartwig, O. Duygulu, L.J. Kecskes, S.N. Mathaudhu, V.H. Hammond, Scripta Mater, 67 (2012) 439-442.

[58] S. Ferrasse, V.M. Segal, F. Alford, J. Kardokus, S. Strothers, Mater Sci Eng A, 493 (2008) 130-140.

[59] V.M. Segal, Mat Sci Eng A, 386 (2004) 269-276.

[60] V.M. Segal, Mat Sci Eng A, 476 (2008) 178-185.

[61] Datasheet 467, Magnesium Elektron UK, Manchester, UK, 2006.

[62] I. Joughin, W. Abdalati, M. Fahnestock, Nature, 432 (2004) 608-610.

[63] H. Lipsitt, R. Baranescu, J. Busch, G. Daehn, L. Howell, M. Mehta, W. Pilkey, O. Sherby, Use of Lightweight Materials in 21st Century Army Trucks, The National Academies Press, Washington, DC, 2003.

[64] L.L. Rokhlin, Magnesium alloys containing rare earth metals : structure and properties, Taylor & Francis, London, 2003.

[65] R.B. Figueiredo, T.G. Langdon, J Mater Sci, 43 (2008) 7366-7371.

[66] H. Watanabe, T. Mukai, K. Ishikawa, K. Higashi, Scripta Mater, 46 (2002) 851-856.

[67] W.J. Kim, H.T. Jeong, Mater Trans, 46 (2005) 251-258.

[68] H. Sun, Y.-N. Shi, M.-X. Zhang, K. Lu, Acta Mater, 55 (2007) 975-982.

[69] H. Lin, J. Huang, T. Langdon, Mater Sci Eng A, 402 (2005) 250-257.

[70] D.C. Foley, M. Al-Maharbi, K.T. Hartwig, I. Karaman, L.J. Kecskes, S.N. Mathaudhu, Scripta Mater, 64 (2011) 193-196.

[71] A. Yamashita, Z. Horita, T.G. Langdon, Mater Sci Eng A, 300 (2001) 142-147.

[72] N. Stanford, M. Barnett, Mater Sci Eng A, 496 (2008) 399-408.

[73] A. Jain, O. Duygulu, D. Brown, C. Tomé, S. Agnew, Mater Sci and Eng A, 486 (2008) 545-555.

[74] P. Bakarian, Trans of AIME, 147 (1942) 266.

[75] E. Schmid, W. Boas, Plasticity of crystals with special reference to metals, F.A. Hughes, London, 1950.

[76] H. Wainwright, Proc Institution of Mech Eng, 137 (1937) 311-332.

[77] M.M. Avedesian, H. Baker, ASM Specialty Handbook: Magnesium and Magnesium Alloys, ASM International. Materials Park, OH, 1999.

[78] K. Máthis, J. Čapek, Z. Zdražilová, Z. Trojanová, Mater Sci and Eng A, 528 (2011) 5904-5907.

[79] J. Jain, W. Poole, C. Sinclair, M. Gharghouri, Scripta Mater, 62 (2010) 301-304.

[80] Y. Estrin, S.B. Yi, H.G. Brokmeier, Z. Zúberova, S.C. Yoon, H.S. Kim, R.J. Hellmig, Int. J. Mater Res, 99 (2008) 50-55.

[81] M. Hoseini, M. Meratian, M.R. Toroghinejad, J.A. Szpunar, Mater Sci Eng A, 497 (2008) 87-92.

[82] A. Jäger, V. Gärtnerová, Philos Mag Let, 92 (2012) 384-390.

[83] S. Suwas, G. Gottstein, R. Kumar, Mater Sci Eng A, 471 (2007) 1-14.

[84] B. Beausir, S. Suwas, L.S. Tóth, K.W. Neale, J.-J. Fundenberger, Acta Mater, 56 (2008) 200-214.

[85] T. Liu, Y.D. Wang, S.D. Wu, R.L. Peng, C.X. Huang, C.B. Jiang, S.X. Li, Scripta Mat, 51 (2004) 1057-1061.

[86] S. Agnew, J. Horton, T. Lillo, D. Brown, Scripta Mater, 50 (2004) 377-381.

[87] R.B. Figueiredo, P.R. Cetlin, T.G. Langdon, Acta Mater, 55 (2007) 4769-4779.

[88] F. Kang, J.T. Wang, Y. Peng, Mater Sci Eng A, 487 (2008) 68-73.

[89] S. Ding, C. Chang, P. Kao, Metall and Mat Trans A, 40 (2009) 415-425.

[90] P. Molnár, A. Jäger, Philos Mag, 93 (2013).

[91] D. Wilson, J. Chapman, Philos Mag, 8 (1963) 1543-1551.

[92] M. Barnett, Z. Keshavarz, A. Beer, D. Atwell, Acta Mater, 52 (2004) 5093-5103.

[93] M. Meyers, O. Vöhringer, V. Lubarda, Acta Mater, 49 (2001) 4025-4039.

[94] D.C. Foley, M. Al-Maharbi, I. Karamar, T. Hartwig, L.J. Kecskes, S. Mathaudhu, Magnesium Technology 2010, Seattle, (2010) 451-454.

[95] D. Brown, S. Agnew, M. Bourke, T. Holden, S. Vogel, C. Tomé, Mater Sci Eng A, 399 (2005) 1-12.

[96] S. Agnew, D. Brown, C. Tomé, Acta Mater, 54 (2006) 4841-4852.

[97] Q. Wang, J.C. Gao, W.J. Niu, Light Metals Tech, 618 (2009) 191-194.

[98] I. Beyerlein, L. Capolungo, P. Marshall, R. McCabe, C. Tomé, Philos Mag, 90 (2010) 2161-2190.

[99] A. Ghaderi, M.R. Barnett, Acta Mater, 59 (2011) 7824-7839.

[100] J. Wang, L. Liu, C. Tomé, S. Mao, S. Gong, Mater Res Let, 1 (2013) 81-88.

[101] G. Proust, C.N. Tomé, A. Jain, S.R. Agnew, Int J Plasticity, 25 (2009) 861-880.

[102] M. Knezevic, A. Levinson, R. Harris, R.K. Mishra, R.D. Doherty, S.R. Kalidindi, Acta Mater, 58 (2010) 6230-6242.

[103] W. Hartt, R. Reed-Hill, Trans Metall Soc AIME, 242 (1968) 1127-1133.

[104] L. Meng, P. Yang, Q. Xie, W. Mao, Mater Trans, 49 (2008) 710-714.

[105] O. Muránsky, M. Barnett, D. Carr, S. Vogel, E. Oliver, Acta Mater, 58 (2010) 1503-1517.

[106] M. Barnett, Scripta Mater, 59 (2008) 696-698.

[107] M. Li, T. Tamura, K. Miwa, Acta Mater, 55 (2007) 4635-4643.

[108] A. Hellawell, P.M. Herbert, Proc Royal Soc London A, 269 (1962) 560-573.

[109] M. Pozuelo, C. Melnyk, W.H. Kao, J.-M. Yang, J Mater Res, 26 (2011) 904-911.

[110] Y. Wang, H. Xu, D.L. Erdman, M.J. Starbuck, S. Simunovic, Adv Eng Mater, 13 (2011) 943-948.

[111] G. Davies, Materials for automobile bodies, Butterworth-Heinemann, Oxford, 2012.

[112] G.-L. Song, JOM, 64 (2012) 671-679.

[113] S. Ferrasse, V.M. Segal, K.T. Hartwig, R.E. Goforth, Metall Mater Trans A, 28 (1997) 1047-1057.

[114] V. Hammond, S. Mathaudhu, K. Doherty, S. Walsh, L. Vargas, B. Placzankis, J. Labukas, M. Pepi, M. Trexler, B. Barnett, Ultrahigh-Strength Magnesium Alloys for the Future Force: A Final Report on the 5-Year Mission Program, 2009-2013, US ARL, Aberdeen Prooving Ground, MD, 2014.

[115] J.D. Robson, N. Stanford, M.R. Barnett, Acta Mater, 59 (2011) 1945-1956.

APPENDIX A

VITA

David Christopher Foley was born in Dallas, TX. He received his Bachelor of Science degree in Engineering Science from Trinity University in San Antonio, TX. He received his Master of Science in Mechanical Engineering from Texas A&M University in College Station, TX.

David may be contacted through the Materials Science and Engineering Department, Texas A&M University, College Station, TX 77843 or by rubbing two small stones together while whistling the chorus to "Tiny Dancer" by Elton John.